

## V899 Mon: a peculiar eruptive young star close to the end of its outburst

SUNKYUNG PARK,<sup>1</sup> ÁGNES KÓSPÁL,<sup>1,2,3</sup> FERNANDO CRUZ-SÁENZ DE MIERA,<sup>1</sup> MICHAŁ SIWAK,<sup>1</sup> MAREK DRÓŹDŹ,<sup>4</sup>  
BERNADETT IGNÁ CZ,<sup>1</sup> DANIEL T. JAFFE,<sup>5</sup> RÉKA KÖNYVES-TÓTH,<sup>1</sup> LEVENTE KRISKOVICS,<sup>1</sup> JAE-JOON LEE,<sup>6</sup>  
JEONG-EUN LEE,<sup>7</sup> GREGORY N. MACE,<sup>5</sup> WALDEMAR OGŁOZA,<sup>4</sup> ANDRÁS PÁL,<sup>1</sup> STEPHEN B. POTTER,<sup>8,9</sup>  
ZSÓFIA MARIANNA SZABÓ,<sup>1,10</sup> RAMOTHOLO SEFAKO,<sup>8</sup> AND HANNAH L. WORTERS<sup>8</sup>

<sup>1</sup>*Konkoly Observatory, Research Centre for Astronomy and Earth Sciences, Eötvös Loránd Research Network (ELKH), Konkoly-Thege Miklós út 15-17, 1121 Budapest, Hungary*

<sup>2</sup>*Max Planck Institute for Astronomy, Königstuhl 17, 69117 Heidelberg, Germany*

<sup>3</sup>*ELTE Eötvös Loránd University, Institute of Physics, Pázmány Péter sétány 1/A, 1117 Budapest, Hungary*

<sup>4</sup>*Mount Suhora Astronomical Observatory, Cracow Pedagogical University, ul. Podchorążych 2, 30-084 Kraków, Poland*

<sup>5</sup>*Department of Astronomy, University of Texas at Austin, 2515 Speedway, Austin, TX, USA*

<sup>6</sup>*Korea Astronomy and Space Science Institute 776, Daedeok-daero, Yuseong-gu, Daejeon, 34055, Republic of Korea*

<sup>7</sup>*School of Space Research, Kyung Hee University 1732, Deogyong-daero, Giheung-gu, Yongin-si, Gyeonggi-do, 17104, Republic of Korea*

<sup>8</sup>*South African Astronomical Observatory, PO Box 9, Observatory 7935, South Africa*

<sup>9</sup>*Department of Physics, University of Johannesburg, PO Box 524, Auckland Park 2006, South Africa*

<sup>10</sup>*Max-Planck-Institute für Radioastronomie, Auf dem Hügel 69, 53121 Bonn, Germany*

### ABSTRACT

V899 Mon is an eruptive young star showing characteristics of both FUors and EXors. It reached a peak brightness in 2010, then briefly faded in 2011, followed by a second outburst. We conducted multi-filter optical photometric monitoring, as well as optical and near-infrared spectroscopic observations of V899 Mon. The light curves and color-magnitude diagrams show that V899 Mon has been gradually fading after its second outburst peak in 2018, but smaller accretion bursts are still happening. Our spectroscopic observations taken with Gemini/IGRINS and VLT/MUSE show a number of emission lines, unlike during the outbursting stage. We used the emission line fluxes to estimate the accretion rate and found that it has significantly decreased compared to the outbursting stage. The mass loss rate is also weakening. Our 2D spectro-astrometric analysis of emission lines recovered jet and disk emission of V899 Mon. We found the emission from permitted metallic lines and the CO bandheads can be modeled well with a disk in Keplerian rotation, which also gives a tight constraint for the dynamical stellar mass of  $2 M_{\odot}$ . After a discussion of the physical changes that led to the changes in the observed properties of V899 Mon, we suggest this object is finishing its second outburst.

*Keywords:* Young stellar objects — FU Orionis stars — Circumstellar disks — Multi-color photometry — Photometry — Spectroscopy — Young stellar objects — Light curves

### 1. INTRODUCTION

Throughout low-mass star formation, the material is transferred from the surrounding envelope to the protostellar disk via infall motion. Then, the material is accreted onto a central protostar until the final stages of the star-forming process. A constant replenishing of material from the envelope onto the disk is needed to sustain the accretion rate for the growth of the proto-

star. The mass accretion rate was originally thought to be constant ( $\sim 2 \times 10^{-6} M_{\odot} \text{ yr}^{-1}$ ; Shu 1977), however, observations show that the luminosities of young stellar objects (YSOs) are about ten times lower than required by the standard accretion model. This discrepancy of the luminosity is known as the luminosity problem (Kenyon et al. 1990; Dunham et al. 2010), and episodic accretion is suggested as a possible solution (Audard et al. 2014, and references therein). In this scenario, protostars stay mostly in their quiescent-accretion phases (which explains the observed low luminosities), while their mass accretion is dominated by a relatively brief phase of episodic bursts.

Eruptive YSOs are observable evidence of enhanced accretion rates undergoing large amplitude accretion outbursts. The outbursts, attributed to highly enhanced accretion from the disk to the central protostar, play an important role not only in the growing mass of the central protostar but also in the evolution of the circumstellar disk. Based on their light curves and spectroscopic properties, eruptive YSOs are classified as FU Orionis-type objects (FUors) or EX Lupi-type objects (EXors).

FUors brighten by more than 4 magnitudes in the optical domain and remain in their brightened state for several decades. Spectroscopic characteristics are P Cygni profiles in H $\alpha$  6563 Å, broad blue-shifted absorption profiles of H $\beta$  4861 Å, Fe II 5018 Å, Mg I 5183 Å, and Na I D 5890/5896 Å doublet, broad and strong CO overtone bandhead absorption features, triangular H band continuum shape, and wavelength-dependent spectral types ranging from F/G supergiants in visual bands to K/M supergiants in near-infrared (NIR). In FUors spectra, emission lines are rarely present except for the P Cygni profiles (Hartmann & Kenyon 1996; Herbig et al. 2003; Audard et al. 2014; Connelley & Reipurth 2018).

EXors also brighten by a few magnitudes, but unlike FUors, they remain in the high brightness stage for a few months to a few years. Observations of repetitive outbursts are almost the rule for the majority of EXors, e.g., EX Lup (Rigliaco et al. 2020) and V1647 Ori (Ninan et al. 2013). Another major difference between the two classifications is the rich emission line spectrum found in EXors (Herbig 2007; Aspin et al. 2010; Kóspál et al. 2011a; Audard et al. 2014; Hodapp et al. 2019, 2020).

V899 Mon (also known as IRAS 06068-0641;  $\alpha_{J2000}=06^{\text{h}} 09^{\text{m}} 19^{\text{s}}24$ ,  $\delta_{J2000}=-6^{\circ} 41' 55''89$ ), is an eruptive young star which shows photometric and spectroscopic characteristics of both FUors and EXors. It is located near the Monoceros R2 molecular cloud, at a distance of  $809 \pm 17$  pc (Gaia Collaboration et al. 2021). V899 Mon was classified as flat-spectrum or an early Class II object (Greene et al. 1994). The outburst of this star was first noticed on 2009 November 10 by Wils et al. (2009), and follow-up spectroscopic and photometric monitoring observations were conducted by Ninan et al. (2015). The brightness peak of the first outburst was observed in 2010, and then it went back to quiescence for a relatively short period ( $< 1$  yr) in 2011. Afterwards, it brightened again in 2012 (see Figure 7 in Ninan et al. (2015) and Figure 1). In their spectroscopic monitoring observations, a number of emission lines and several P Cygni profiles are observed in V899 Mon. The high-velocity absorption components of the P Cygni profiles are varied with time.

The physical parameters of V899 Mon (Table 1) were constrained by Ninan et al. (2015). The peak accretion rate of  $10^{-6} M_{\odot} \text{ yr}^{-1}$  is typical for EXors (Audard et al. 2014, and references therein), however, FUors can have comparable values (e.g., Kóspál et al. 2011b). A relatively short period of the brightened stage, repetitive outbursts, and rich emission lines are characteristics of EXors. Overall, the derived photometric and spectroscopic properties are in between the FUors and EXors but show more similarity to EXors. Ninan et al. (2016) studied the variation of the high-velocity component of outflowing wind and concluded that the outflow is driven by magnetospheric accretion. Kóspál et al. (2020) analyzed the mid-infrared  $10 \mu\text{m}$  silicate emission feature of V899 Mon, and found this target is in the Class II stage with signs of significant grain growth. Recently, Kóspál et al. (2021) performed ALMA 1.3 mm continuum observation and radiative transfer modeling to investigate the disk properties. The derived disk mass of  $0.03 M_{\odot}$  is the lowest among the 10 FUors analyzed by the authors. Furthermore, by comparing the disk mass with the stellar mass (Table 1), the authors found the disk around V899 Mon does not fall within the region of gravitational instability. This mechanism has been suggested as the trigger behind FUor-type outbursts (Audard et al. 2014), thus it is likely the episodic accretion of V899 Mon experiences a different triggering mechanism.

In this study, we characterize the current physical properties of V899 Mon by analyzing new and archival photometric and spectroscopic data. New observations and the data reduction, as well as used archival data, are described in Section 2. In Section 3, we present the period and color magnitude analyses of photometric observations, as well as spectral analysis and disk modeling results. In Section 4, we discuss our results and compare them with those from previous studies. Finally, we summarize our results and findings in Section 5.

## 2. OBSERVATIONS AND DATA REDUCTION

### 2.1. Optical Photometry

We obtained ground-based optical photometric observations of V899 Mon between 2017 November and 2021 May with different telescopes around the world (Figure 1). At the Piszkestető Mountain Station of Konkoly Observatory (Hungary), we used two telescopes. The first one is a 60/90/180 cm Schmidt telescope, equipped with an Apogee Alta U16 CCD camera,  $1''.027$  pixel scale,  $70'.0 \times 70'.0$  field of view, Johnson-Cousins  $BVR_CI_C$  filters. The second one is a 80 cm Ritchey-Chretien (RC80) telescope equipped with an FLI PL230 CCD camera,  $0''.55$  pixel scale,  $18'.8 \times 18'.8$

**Table 1.** Target Information

	Parameters	Reference
$V_{\text{LSR}}$	9.63 km s <sup>-1</sup>	1
Distance	809.20 ± 17.08 pc	2
$A_V$	2.6 mag	3
$M_*$	~ 2 $M_{\odot}$	1, 3
$M_{\text{disk}}$	0.03 $M_{\odot}$	4
$R_*$	4 $R_{\odot}$ , 6 $R_{\odot}$	3, 4
$R_{\text{disk}}$	19 ± 5 $R_{\odot}$	4
age	1 ~ 5 Myr	3
$i$	41 ~ 58 °	1, 4
$L_{\text{bol}}$ (outburst)	~ 150 $L_{\odot}$	3
$L_{\text{bol}}$ (2020 Sep.)	~ 21 $L_{\odot}$	1
$\dot{M}_{\text{acc}}$ (outburst)	10 <sup>-8</sup> ~ 10 <sup>-6</sup> $M_{\odot}$ yr <sup>-1</sup>	3
$\dot{M}_{\text{acc}}$ (2020 Sep.)	~ 2 × 10 <sup>-7</sup> $M_{\odot}$ yr <sup>-1</sup>	1
$\dot{M}_{\text{out}}$ (outburst)	~ 2.6 × 10 <sup>-7</sup> $M_{\odot}$ yr <sup>-1</sup>	3
$\dot{M}_{\text{out}}$ (2020 Sep.)	~ 2.1 × 10 <sup>-8</sup> $M_{\odot}$ yr <sup>-1</sup>	1

**References**— (1) This Work; (2) Gaia Collaboration et al. (2021); (3) Ninan et al. (2015); (4) Kóspál et al. (2021)

field of view, and Johnson  $BV$  and Sloan  $g'r'i'$  filters. At the Mount Suhora Observatory (MSO) of the Cracow Pedagogical University (Poland), we used the 60 cm Carl-Zeiss telescope equipped with an Apogee Aspen-47 camera, 1''116 pixel scale, 19'0 × 19'0 field of view, and Sloan  $g'r'i'$  filters. At the South African Astronomical Observatory (SAAO), we used Lesedi, the new SAAO 1-m telescope, equipped with a Sutherland High Speed Optical Camera (SHOC), 2x2 binning, 0''666 pixel scale, 5'7 × 5'7 field of view, and Bessel  $UBVR_CI_C$  filters. At Adiyaman University Observatory (Turkey), we used ADYU60, a PlaneWave 60 cm f/6.5 corrected Dall-Kirkham Astrograph telescope, equipped with an Andor iKon-M934 camera, 0''673 pixel scale, 11'5 × 11'5 field of view, Sloan  $g'r'i'$  filters. During December, 2020 and January 2021 we also observed V899 Mon by means of OMEGACAM installed on VST, as a part of our ESO programme ID 106.21LL (PI: Siwak). The camera covers 1×1 deg field in  $u'g'r'i'z'$  filters.

During the observing nights, typically 3 to 10 images of V899 Mon were taken in each filter. After standard reduction on bias, flat-field, and dark current, we calculated aperture photometry for the science target and several comparison stars in the field of view using an aperture radius of 5''. We selected the comparison stars from the APASS9 catalog (Henden et al. 2015), which provides Bessel  $BV$  and Sloan  $g'r'i'$  magnitudes for the potential comparison stars. We calculated the  $R_C$  and  $I_C$  magnitudes of the comparison stars by plotting their broad-band SED using their APASS9 and 2MASS magnitudes (Cutri et al. 2003) and spline interpolating for the effective wavelengths of the  $R_C$  and  $I_C$  filters. We

took  $U$  band magnitudes for the comparison stars from the Swift/UVOT Serendipitous Source Catalog (Yershov 2014). We used the comparison stars for the photometric calibration by fitting a linear color term. Magnitudes taken with the same filter on the same night were averaged. The final uncertainties are the quadratic sum of the formal uncertainties of the aperture photometry, the photometric calibration, and the scatter of the individual magnitudes that were averaged per night. The results can be found in Table 5 in the Appendix A.

In addition to our data, we utilize the public-domain ASAS-SN  $V$  and  $g$  (Shappee et al. 2014; Kochanek et al. 2017), and ZTF  $g'r'$  (Masci et al. 2018) light curves extracted and calibrated to standard photometric systems by means of dedicated pipelines. These surveys provide data obtained with the typical cadence of 1 day, though one can identify periods with two or more visits per night. The ASAS-SN data utilized in this work were obtained between 2012 February 5 (although the major time-series has started on 2014 December 16) and 2021 May 17, while the ZTF data between 2018 January 9 – 2021 January 19.

Finally, to enable the first insights into the small-scale variability unavailable for detailed investigation from the ground, we extracted the light curve from the calibrated full-field images (FFI) obtained with 10 min (0.00694436 d) cadence by TESS (Ricker et al. 2015) during 2020 December 18 – 2021 January 13 (Sector 33). Aperture size of 2 pixels was used to extract the stellar flux (Figure 2). The total monitoring time was 25.83304 d, with only 1.57642 d break in the middle of the run, necessary for the data transfer to the ground.

## 2.2. Infrared WISE Photometry

In order to construct a mid-infrared light curve of V899 Mon, we downloaded single exposure data taken by the WISE mission (Wright et al. 2010) from the AllWISE Multiepoch Photometry Table and the NEOWISE-R Single Exposure (L1b) Source Table. We used only the best quality data points and discarded low quality measurements ( $qi\_fact < 1$ ). Following Section 2.3 of the Explanatory Supplement (Cutri et al. 2015), we filtered out data that could be contaminated by higher levels of charged particle hits due to the satellite being close to the South Atlantic Anomaly ( $saa\_sep < 5$ ). We checked that none of the data points come from regions contaminated by scattered light from the moon ( $moon\_masked = 1$ ). Finally, we rejected data points where the reduced  $\chi^2$  of the profile-fit photometry measurement ( $w1rchi2$  or  $w2rchi2$ ) was higher than 100. Being in the 5–7 mag mid-infrared brightness range, the WISE photometry of V899 Mon was affected by satu-

ration. We corrected the individual data points for saturation using the correction curves given in Section 2.1 of the Explanatory Supplement. We then calculated the average and standard deviation of the data points for each observing season and found that the scatter was less than or similar to the uncertainty of the individual magnitudes. Therefore, in the following, we use the seasonal averages.

### 2.3. Optical Spectroscopy

Optical integral field spectroscopic observations were conducted for V899 Mon using the Multi Unit Spectroscopic Explorer (MUSE; Bacon et al. 2010) on the Very Large Telescope at Paranal Observatory (Chile). The data were taken on 2021 January 22, as part of our ESO programme ID 106.21KL (PI: Cruz-Sáenz de Miera). The observations were carried out with the WFM-AO-N mode. The Wide Field Mode (WFM) provides a  $60'' \times 60''$  field of view (FOV) with a pixel size of  $0.2'' \times 0.2''$ . The MUSE nominal mode (N) provides a wavelength coverage between 4800 Å and 9300 Å with a resolving power between 1770 and 3590. Due to the Na Notch filter of the adaptive optics (AO) system (Arsenault et al. 2008; Ströbele et al. 2012), there is a gap in spectral coverage between 5820 Å and 5970 Å.

The observations were executed in six 126 second exposures each with a total integration time of 12.6 minutes on V899 Mon. Each exposure was dithered by  $\sim 1''$ , and rotated by  $90^\circ$ . The individual exposures were performed with a clear sky transparency and a seeing between  $0.89''$  and  $1.10''$ . The observations were reduced using the MUSE pipeline (version 2.8.4; Weilbacher et al. 2020) by ESO, resulting in a fully calibrated and combined MUSE data cube with the instrumental signature and the sky background removed. The S/N around H $\alpha$  6563 Å is about 50.

The spectrum was extracted using a  $5''$  circular aperture positioned on the peak of the stellar emission. Then, the the spectrum was shifted by the barycentric velocity of  $-12.96 \text{ km s}^{-1}$  calculated by barycorrpy (Wright & Eastman 2014) and by the systemic velocity of  $9.63 \text{ km s}^{-1}$  ( $V_{\text{LSR}}$ ) obtained from the ALMA C $^{18}\text{O}$  line data (Appendix B). The systemic velocity in the heliocentric system ( $V_{\text{helio}}$ ) converted from  $V_{\text{LSR}}$  is  $27.92 \text{ km s}^{-1}$ .

### 2.4. Near-infrared Spectroscopy

The NIR spectrum of V899 Mon was obtained with Immersion GRating INfrared Spectrograph (IGRINS) installed on the 8.1m Gemini South telescope on 2020 November 6. IGRINS provides high-resolution ( $R \sim 45,000$ ; corresponding to a velocity resolution of

$\Delta v \sim 7 \text{ km s}^{-1}$ ) NIR spectra covering the full H (1.49–1.80  $\mu\text{m}$ ) and K (1.96–2.46  $\mu\text{m}$ ) bands with a single exposure (Yuk et al. 2010; Park et al. 2014; Mace et al. 2016). The spectrum was obtained with a slit scale of  $0.34'' \times 5''$ . The S/N of H and K bands are about 244 and 313, respectively. The S/N for each band is the median value per resolution element for the wavelength range of 1.58–1.61  $\mu\text{m}$  and 2.21–2.24  $\mu\text{m}$ . V899 Mon was observed with two series of ABBA nodding observations at different positions on the slit to better subtract the sky background. The exposure time of each nod observation was 300 sec, and the total exposure time was 2,400 sec. A nearby A0 telluric standard star (HD 42133) was observed immediately after the observation of V899 Mon for telluric correction.

The IGRINS pipeline (Lee & Gullikson 2017) was used to reduce the spectra for flat-fielding, sky subtraction, correcting the distortion of the dispersion direction, wavelength calibration, and combining the spectra. Then, telluric correction and flux calibration were performed in the same way as described in Park et al. (2018). Interpolated H and K band magnitudes between our  $BVr'i'$  and NEOWISE data observed in 2020 September were adopted for the flux calibration since there is no recent NIR photometry during the fading state. The barycentric velocity was calculated by the same method as done in the optical spectrum, which is  $19.57 \text{ km s}^{-1}$ . Finally, the barycentric and systemic velocity ( $V_{\text{sys}} = 27.92 \text{ km s}^{-1}$ ) correction was applied.

## 3. RESULTS AND ANALYSIS

### 3.1. Photometry

In order to get a general view on the long term evolution of V899 Mon, in addition to the multi-band light curves shown in Figure 1 we also prepared the "single-band" light curve composed of  $V$ -band data collected from 2009 by Ninan et al. (2015) as well as our own and public-domain  $V$ - and  $g$ -band data. The new data were processed as follows: in order to improve the photon statistic, we averaged typically 3–8 ASAS-SN data points gathered each night in 1-day bins. Outliers were carefully removed prior to this operation. The Schmidt and the most recent RC80 and SAAO  $V$ -band data were included to this dataset without any shifts. In 2018–2019 the ASAS-SN survey gradually switched to the  $g$ -band. We supplemented ASAS-SN light curve with the ZTF, VST, MSO and Adiyaman  $g$ -band data. As the MSO, ASAS-SN, VST and the first two seasons of ZTF  $g$ -band observations do perfectly overlap, we use them as the reference light curves. Only the third season ZTF data required a  $+0.060 \text{ mag}$  shift to match the entire dataset. For the same reason, a  $-0.075 \text{ mag}$  shift was

applied to all Adiyaman  $g$ -band points. We then aligned (with the accuracy of 0.02 mag) the  $g$ -band data to the  $V$ -band data by a constant 0.58 mag shift. As the variability amplitudes are very similar in  $V$ - and  $g$ -bands, no correction on this effect was necessary. The part of the combined light curve, important for the description of the most recent light changes, is shown in Figure 3.

According to Figure 1, V899 Mon is currently fading but it is still brighter than during the 2011 quiescent phase. After the second outburst starting in 2012, the brightness remained at a relatively high level until 2017, reaching the maximum brightness in 2018. After that, it started to gradually fade at the rate of  $0.30 \pm 0.02$  mag yr<sup>-1</sup>, as obtained from linear fit to the recently best sampled  $g$ - and  $V$ -band combined 2016–2021 data. The less numerous ZTF  $r$ -band 2018–2021 data indicate a faster decrease, at a rate of  $0.36 \pm 0.01$  mag yr<sup>-1</sup>.

The evolution of the optical light curve of V899 Mon, however, is far from being smooth. During the early outburst stages, the only feature visible on top of the major light plateau was the major dip in 2011 (Figure 1), which was interpreted as an interruption of the enhanced accretion (Ninan et al. 2015). The rather sparse sampling during 2009–2014 probably hid brightness changes occurring in the time scales of days and weeks, which became visible later, primarily thanks to the almost daily ASAS-SN observations (see the bottom panel in Figure 1 and Figure 3). According to these figures, before 2016, on top of the light plateau caused solely by enhanced accretion we observed rather irregular  $\pm 0.1$  mag light changes. The amplitude of these background oscillations became higher ( $\pm 0.2$  mag) in the 2016/2017 season, when they started to resemble accretion bursts, common for classical T Tauri-type stars (CTTS). The most pronounced  $\Delta V \approx 1$  mag event took place in 2017/2018, and it is marked in red in Figure 3. The entire accretion burst, defined as the rise from and return back to the virtual continuum, lasted for about 200 days. Assuming that the peak duration is in a way related to Keplerian rotation of the disk, the disk warp from which the accretion flow could originate formed roughly at about 1 au from the  $2M_{\odot}$  star. In spite of the large distance, as compared to  $\sim 0.05$ – $0.1$  au in ordinary CTTS, this view seems to be supported by the presence of the central dip (marked in blue in Figure 3). It is similar to observed in other CTTS, in which during favorable viewing geometry, the optically thick part of the accretion column is causing total or partial occultations of hot spots created on the stellar photosphere (Siwak et al. 2018). In the case of V899 Mon, the eclipse of the associated hot spot appears to be total.

In 2020/2021 another well-defined accretion burst with accompanying central dip appeared. It lasted for about 30 days, which suggests that it originated from a disk warp that formed at  $\sim 0.2$  au from the star. This value is closer to low-massive CTTS, where the accretion flow originates near the disk co-rotation radius.

Accretion bursts of smaller amplitudes are visible at other epochs as well, in addition to apparently random  $V \approx 0.5$  mag dips. These dips are not obviously connected to accretion bursts but may result from dusty clouds passing in front of the bright inner disk and/or the star itself.

### 3.1.1. Period analysis of ground-based data

In order to investigate variability occurring on timescales from days to months, we utilize the  $V$ - and  $g$ -band data providing the longest and most uniform temporal coverage (Figure 3, and see the description in the previous paragraph).

Using the generalised Lomb-Scargle periodogram (Zechmeister & Kürster 2009), we started from unsuccessful attempt to search for periodic variations in the entire data set. This failure, however, is mostly caused by changing morphology of the light curve and the yearly breaks in the data acquisition. Therefore in the second attempt, we decided to analyze each season separately. The seasonal trends visible in the data were removed prior to the analysis by simple 2–3 order polynomial fits. We found that there is no quasi-periodicity persistent for one full observing season. This is better illustrated by the spectrum obtained by means of the weighted wavelet Z-transform (WWZ, Foster 1996), designed for analysis of unevenly sampled light curves and available within the VARTOOLS package (Hartman & Bakos 2016, Figure 4). We show the WWZ spectrum only for one season, but those obtained for other seasons look similar. They do contain information about spacing between dips and accretion bursts, and a mixture of other small-scale variabilities, which should be treated with caution and always accompanied by simultaneous viewing of light curves. The spectra do reveal that both the accretion burst- and the dip-related quasi-periodic oscillation last for 2–3 oscillatory cycles and then disappear. In the case of accretion burst, this behavior is typical for unstable or moderately-stable accretion (e.g., Blinova et al. 2016).

### 3.1.2. Period analysis of TESS data

In order to get a detailed look into the shortest variability time scales, we performed a frequency analysis of the 26 day-long TESS light curve obtained during 2020 December 16 – 2021 January 11 (Figure 2). The

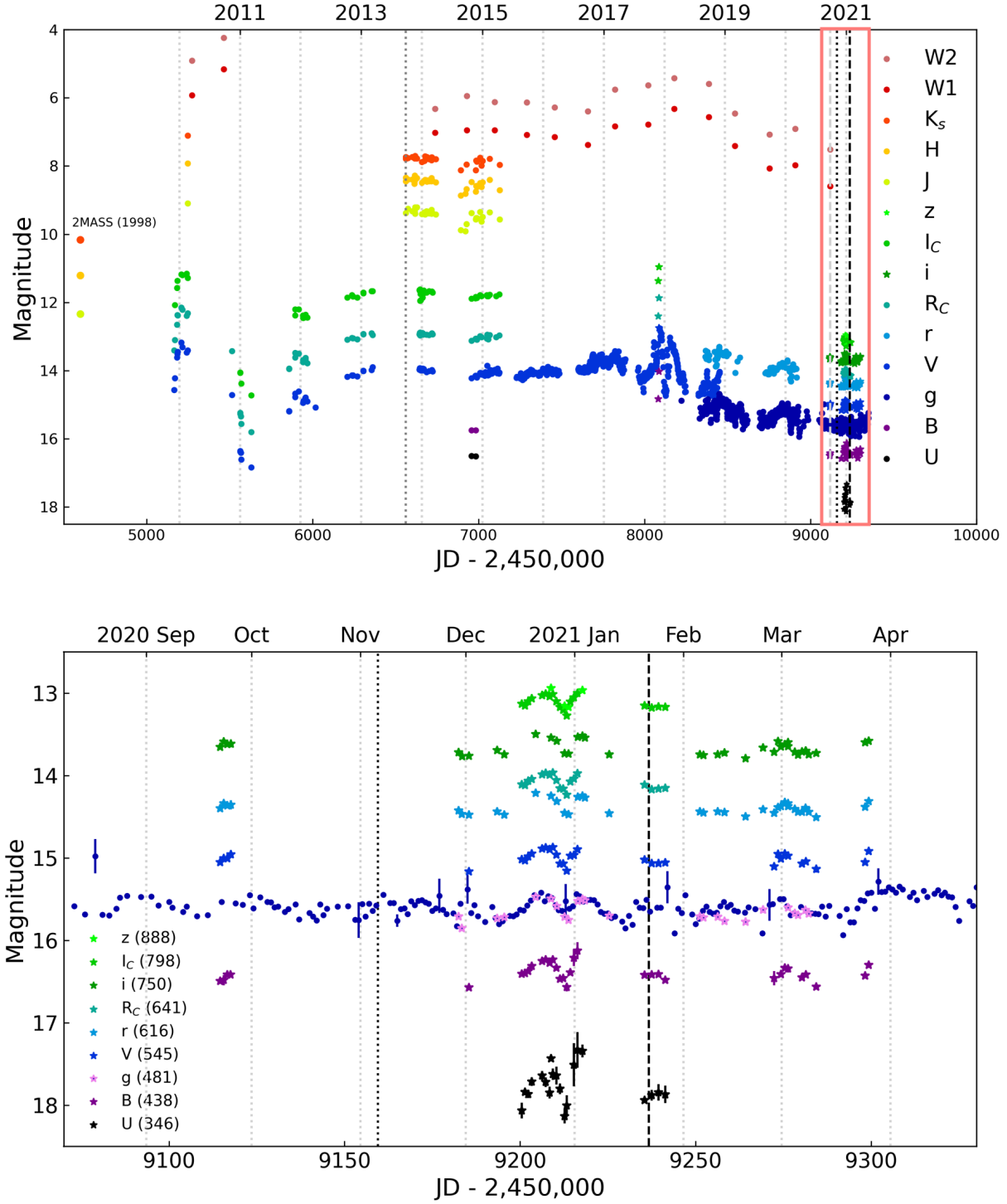


**Figure 1.** Top: light curve of V899 Mon. Bottom: light curve of V899 Mon for the 2020 September – 2021 April time period (pink box in the top panel). The bottom figure shows our own observations from Table 5 (Appendix A), complemented with data from the ASAS-SN survey. The photometric uncertainty smaller than the symbol size is not presented. The numbers in brackets indicate the central wavelength of each filter in nm. The photometric data from the ASAS-SN (V and g; Shappee et al. 2014; Kochanek et al. 2017), ZTF (g and r; Masci et al. 2018), WISE (W1 and W2; Mainzer et al. 2011), 2MASS (J, H, K<sub>s</sub>; Cutri et al. 2003), and U, B, V, R, I, J, H, and K<sub>s</sub> from Ninan et al. (2015) were used. Circle and star symbols indicate archival data and our data, respectively. Different colors indicate different bandpasses. The black dotted and dashed lines indicate the spectroscopic observation date of IGRINS and MUSE. The dark gray dotted line in the top panel indicates the observation date of Ninan et al. (2015). Dashed gray line in the top panel indicates the data point used in the SED in Figure 7.

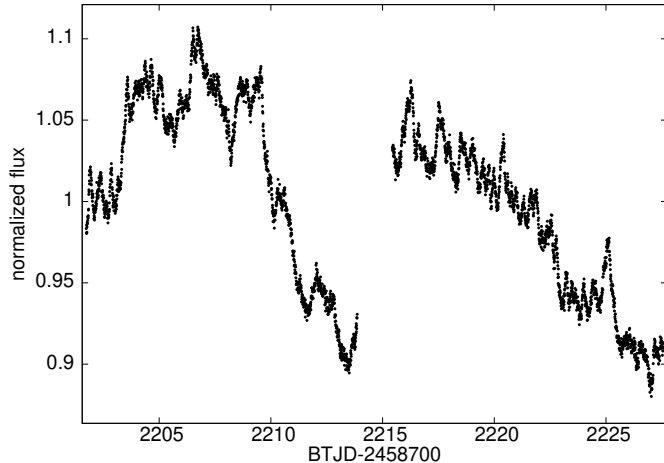


**Figure 2.** TESS light curve of V899 Mon (Sector 33).

amplitude-frequency spectrum does not reveal any well-defined periods, nor quasi-periods (Figure 5). The lack of the outstanding frequencies and the spectrum slope  $a_f \sim f^{-1}$  indicative of the random-walk nature of these light changes (Press 1978) strongly suggest that these stochastic processes are driven by the magnetically-controlled accretion, as in CTTS and some Herbig Ae stars (Rucinski et al. 2010; Stauffer et al. 2014; Siwak et al. 2018). The wavelet analysis also does not reveal any persistent oscillations: there is some indication of a 2.5 d quasi-periodic oscillation in the first half of the light curve, but it disappears after 4–5 cycles and is apparently absent in the second half. Except for the above, both the careful look into the light curve and zoom into the short periodic part of the wavelet spectrum reveals that the shortest accretion bursts have a typical duration time of 0.17 d (4 hr). This enables us to gain even deeper insight into the physical properties of the accretion flow: the disk plasma is not transferred smoothly within the stream but in the form of clumps, a phenomenon first observed in BP Tau (Gullbring et al. 1996), but not yet well understood.

### 3.1.3. Color relations

The long-term color evolution has already been investigated by Ninan et al. (2015). The authors found that the object was reddest during the transition stages from outburst to quiescence and back. Their interpretation was that the outburst had to originate at some place in the disk, like in typical FUors. We show these archival data together with new data points gathered in recent years in Figure 6 a–d.  $V$  vs.  $(V - R)$  and  $V$  vs.  $(V - I)$  color-magnitude diagrams (CMDs) constructed from archival and new data show that although the brightness in 2020/2021 (green symbols) was simi-

lar as during the transition stages from the first peak to the quiescence and back (black symbols), the colors of V899 Mon are currently bluer by 0.25 and 0.6 mag, respectively (Figure 6 c–d).

The major accretion burst (red symbols in Figure 3), which dominated the variability in the 2017/2018 season, was observed only twice in  $BVR_CI_C$  filters of the Schmidt telescope. The respective CMDs (Figure 6 b–d) show that all color indices were significantly bluer when the star was brighter. Although this behavior is similar to that observed in the first outburst in 2010, one should bear in mind that both are caused by different physical mechanisms: during the accretion burst, the color change is caused by the appearance of hot spots on the stellar photosphere, while in 2010 it was caused by the inner disk temperature increase solely through the enhanced accretion.

The same though much better established relation is observed during the 2020/2021 burst. The 2020/2021 data limited to the outburst duration show strong wavelength-dependency during the phenomena: the amplitude ( $\sim 1$  mag) observed in the  $u$ -filter is about 3–4 times larger than observed by TESS and in remaining filters (Figure 6 e–h). Unfortunately, the SAAO  $U$ -band data turned out to be too noisy to demonstrate this effect with similar precision as the ESO data. The accretion burst amplitude in  $g$ -band reached barely 0.25 mag, and is only slightly smaller in  $z$ -band (Figure 6 f).

## 3.2. Spectroscopy

Optical and NIR spectroscopic observations were taken in 2021 January and 2020 November, respectively. To put our spectra into context, in Figure 7 we show the SED of V899 Mon with our observations and those from Ninan et al. (2015). Our photometric (black crosses) and spectroscopic (gray line) observations were conducted in the brightness between the outburst and quiescent phases. We calculated the bolometric luminosity ( $L_{\text{bol}}$ ) using our optical photometry and NEOWISE data obtained in September 2020 and JHK interpolated by optical and NEOWISE. For FIR data, quiescent data of Ninan et al. (2015) were used. The obtained  $L_{\text{bol}}$  is  $21 L_{\odot}$ ; the lower  $L_{\text{bol}}$  indicates that V899 Mon is in the fading state compared to the outbursting stage ( $\sim 150 L_{\odot}$ ; Ninan et al. 2015).

Figure 8 shows optical and NIR spectrum of V899 Mon with rich emission lines. In the following subsections, we discuss the various spectral features observed in V899 Mon.

### 3.2.1. P Cygni profile

In the optical spectrum of V899 Mon,  $H\beta$  4861 Å and  $H\alpha$  6563 Å lines have P Cygni profiles (Figure 9). The

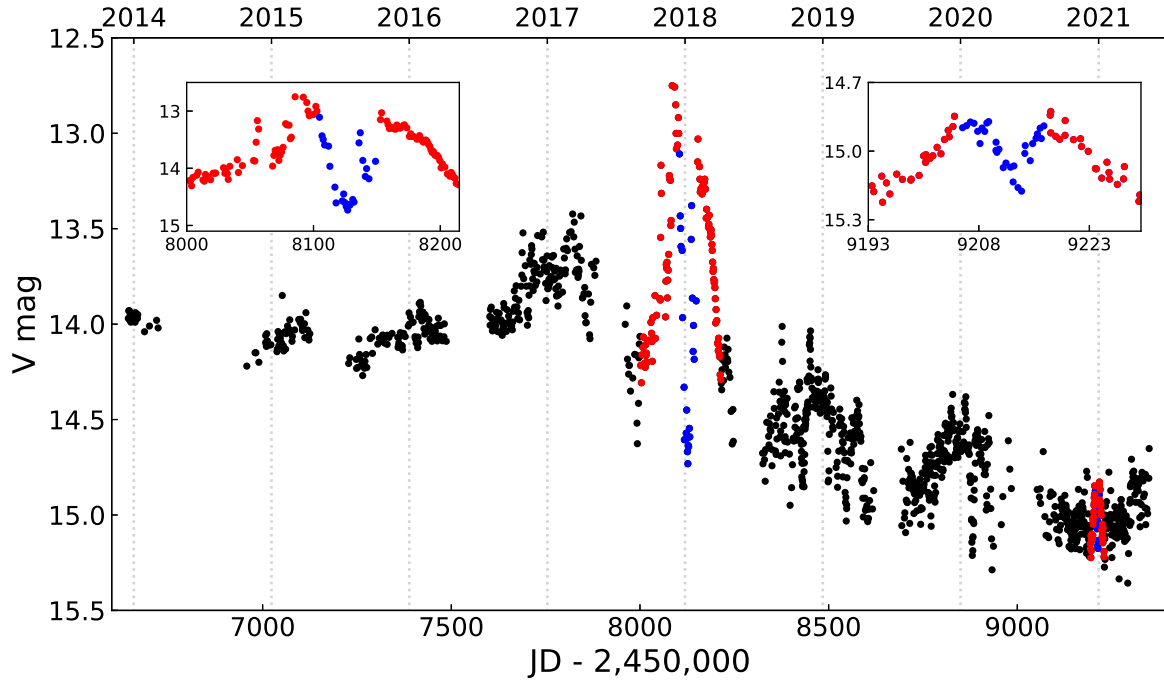


**Figure 3.**  $V$ - and  $g$ -band combined light curve of V899 Mon for the 2014–2021 time period. The two, more widely studied in this paper accretion bursts and accompanying central dips, are indicated by red and blue colors, respectively. Left and right subplots show zoom-in accretion bursts and central dips in 2018 and 2021, respectively.

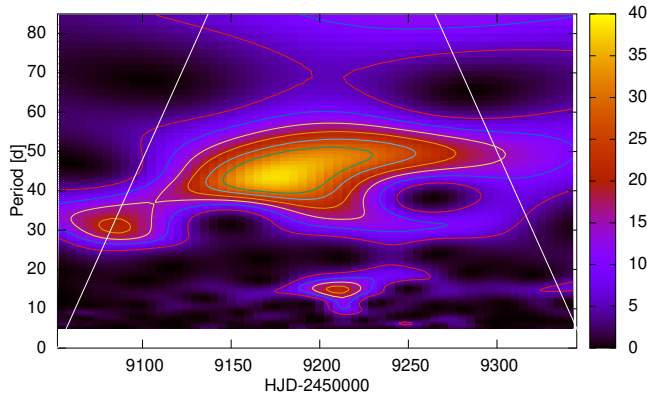


**Figure 4.** WWZ spectrum calculated for 2020/2021 season. The colors represent the Z-statistic values. Edge effects are contained beyond the white lines.

former line shows a relatively stronger blue-shifted absorption component to the latter.  $H\alpha$  shows a shallow blue-shifted absorption component ( $> -332 \text{ km s}^{-1}$  where the intensity is minimum) and a strong emission profile ( $\sim 60 \text{ km s}^{-1}$ ) in our observation (black). The blue-shifted absorption component is produced by an outflowing wind (Hartmann & Kenyon 1996; Hartmann 2009), and typically FUors show strongly blue-shifted

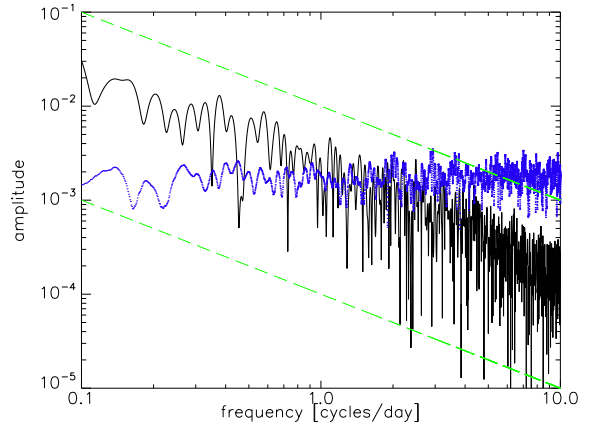


**Figure 5.** Fourier spectrum (black line) of TESS light curve presented in log-log scale. The stochastic nature ( $a_f \sim f^{-1}$ ) of these oscillations is indicated by the two parallel green dashed lines. The amplitude errors are represented by blue dots.

absorption components. Immediately after V899 Mon was discovered,  $H\alpha$  was observed as emission in 2009 November (Wils et al. 2009).  $H\alpha$  showed a strong blue-shifted absorption component of the P Cygni profile in the outbursting state in Ninan et al. (2015) and was also observed as a P Cygni profile in Herczeg et al. (2016). Then the blue-shifted absorption component



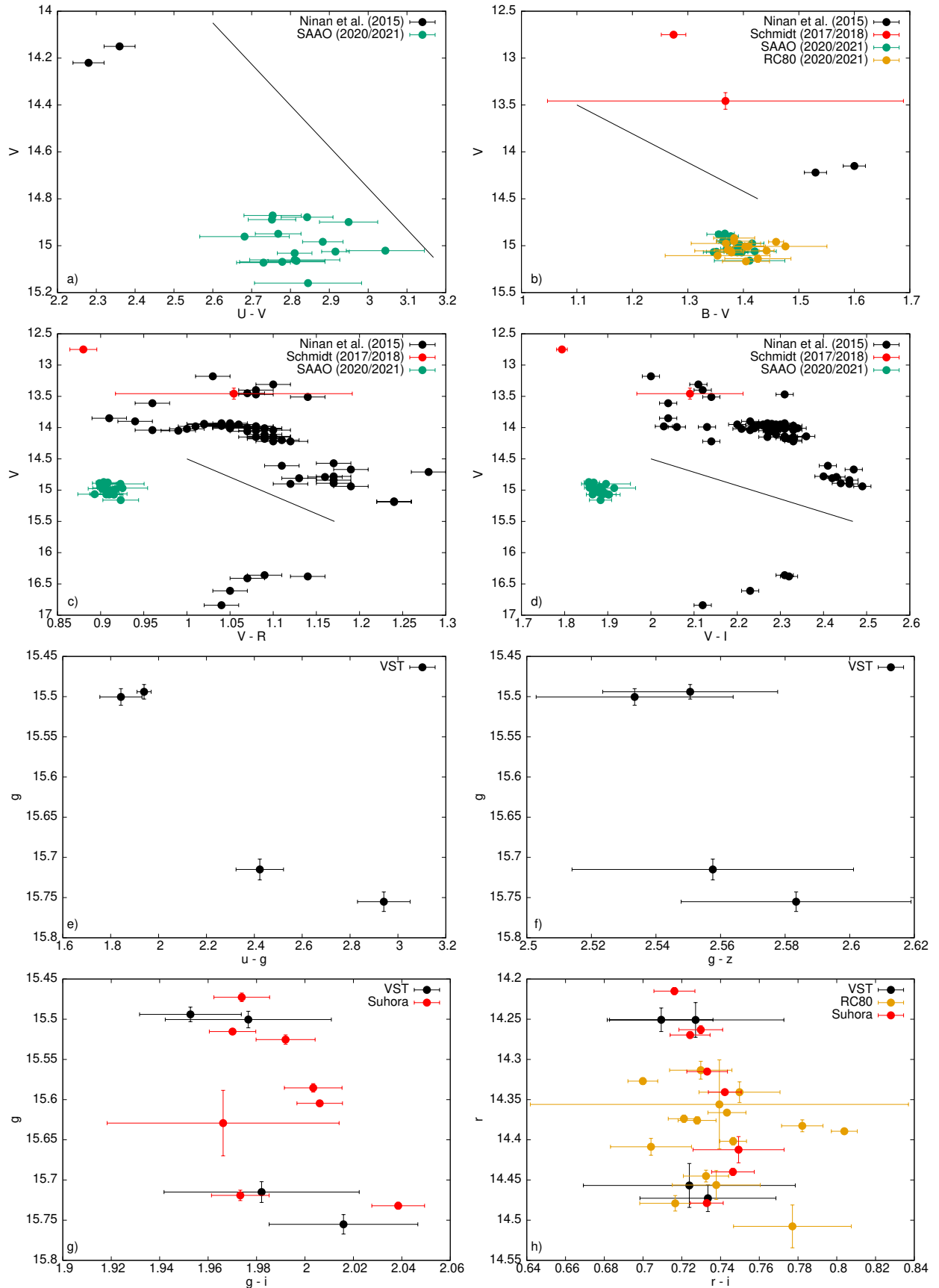


**Figure 6.** Color-magnitude diagrams (CMD) of V899 Mon. Two upper rows (a–d): CMD from the archival and new Johnson filter data. Interstellar reddening vector is indicated by the continuous black line. Two bottom rows (e–h): CMD from the new Sloan filter data.

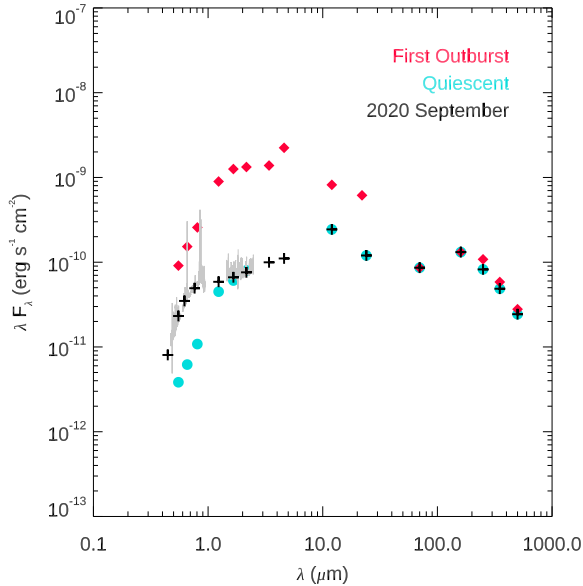


**Figure 7.** SED of V899 Mon. Red diamond and cyan circle symbols represent the first outburst and quiescent states from Ninan et al. (2015). Black cross symbol indicates our  $BVr'i'$  observation and NEOWISE (W1 and W2; Mainzer et al. 2014) data observed in 2020 September (dashed gray line in the top panel in Figure 1).  $JHK$  data points are interpolated between optical and NEOWISE data. For data longer than  $10 \mu\text{m}$ , the quiescent phase data (Ninan et al. 2015) are plotted. Our spectroscopic observations (gray line) were obtained at an intermediate brightness state between the outburst and quiescent phases.

became weaker as V899 Mon faded. A nearly symmetric profile of  $H\alpha$  was observed in the quiescent phase (Figure 17 in Ninan et al. 2015), and our observations recovered a similar profile.

According to previous studies (Ninan et al. 2015, 2016), Ca II IRT lines also showed P Cygni profiles during the outbursting stage and evolved similarly to  $H\alpha$ . In our observation, Ca II shows only symmetric emission profiles (Figure 10). Combined with the  $H\alpha$  line profile, the weakening of the blue-shifted absorption component of the P Cygni profiles indicates that the strength of the outflowing wind became weaker compared to the outbursting stage.

The line ratio of  $H\alpha/H\beta$  in our observation is about 18, which is 2 or 3 times higher than the ratio found by Ninan et al. (2015). The higher ratio in our observation also indicates the weakening of the outflowing wind based on the line profile of  $H\alpha$ .

### 3.2.2. Ca II IRT lines

As mentioned in Section 3.2.1, Ca II IRT lines were observed in emission ( $\text{FWHM} > 162 \text{ km s}^{-1}$ , Figure 10).

This feature is often seen in CTTS and is interpreted as originating in the magnetospheric accretion (Muzerolle et al. 1998), also seen in EXors (Herbig 2008; Sipos et al. 2009; Sicilia-Aguilar et al. 2012; Hillenbrand et al. 2019; Hodapp et al. 2019, 2020), and V1647 Ori (Aspin et al. 2010; Aspin 2011; Ninan et al. 2013).

The intensity ratio between the Ca II IRT emission lines is nearly equal, 1.06:1.00:0.86, which suggests optically thick emission (Herbig & Soderblom 1980; Hamann & Persson 1992; Azevedo et al. 2006). This ratio is similar to the previous study (1:1.01:0.77; Ninan et al. 2015), and also similar to CTTS (Herbig & Soderblom 1980; Hamann & Persson 1992), EXors (Hodapp et al. 2019, 2020), and V1647 Ori (Ninan et al. 2013). While the line ratio is similar to that of the outbursting stage, the relative intensity of the  $8498 \text{ \AA}$  line became stronger. The strength of the  $8542 \text{ \AA}$  line should be the strongest according to the transition probability, but the opposite trend ( $8498 \text{ \AA} > 8542 \text{ \AA}$ ) is also observed in many CTTS (Hamann & Persson 1992). In this case, the width of  $8498 \text{ \AA}$  is smaller than that of  $8542 \text{ \AA}$ , and the widths of  $8542 \text{ \AA}$  and  $8662 \text{ \AA}$  are similar. The intensity ratios and line profiles of Ca II IRT of V899 Mon show similarity to CTTS.

### 3.2.3. Permitted atomic lines

A number of permitted atomic emission lines are observed in the optical and NIR spectra of V899 Mon similar to CTTS (Muzerolle et al. 1998), EXors (Lorenzetti et al. 2009; Kóspál et al. 2011a; Sicilia-Aguilar et al. 2012; Hodapp et al. 2019, 2020), and V1647 Ori (Fedele et al. 2007; Aspin 2011; Ninan et al. 2013). The observed lines are marked in Figure 8: C I, Fe I, He I, Cr I, Ti I, Ca I, Th I, K I, Cl I, O I, Mg I, Si I, and Na I. The line flux of the relatively strong and isolated lines is measured and listed in Table 2. Optical lines are observed with single Gaussian profiles, while NIR lines are resolved with double-peaked line profiles. Figure 11 shows NIR asymmetric double-peaked line profiles. We measured the half-width at half-depth (HWHD; Petrov & Herbig 2008) of each blue-shifted and red-shifted wing because of the line asymmetry. Figure 12 shows the measured HWHD as a function of wavelength. Na I  $2.2062 \mu\text{m}$  line is blended by Si I  $2.2069 \mu\text{m}$  line; therefore, we did not measure the HWHD of this line. A general trend of HWHD decreases with increasing wavelength, suggesting that these atomic lines are formed at the disk (Zhu et al. 2009; Lee et al. 2015; Park et al. 2020).

### 3.2.4. Forbidden lines

We detected numerous forbidden emission lines in V899 Mon. This makes it more similar to EXors or CTTS rather than FUors (Hamann & Persson 1992;

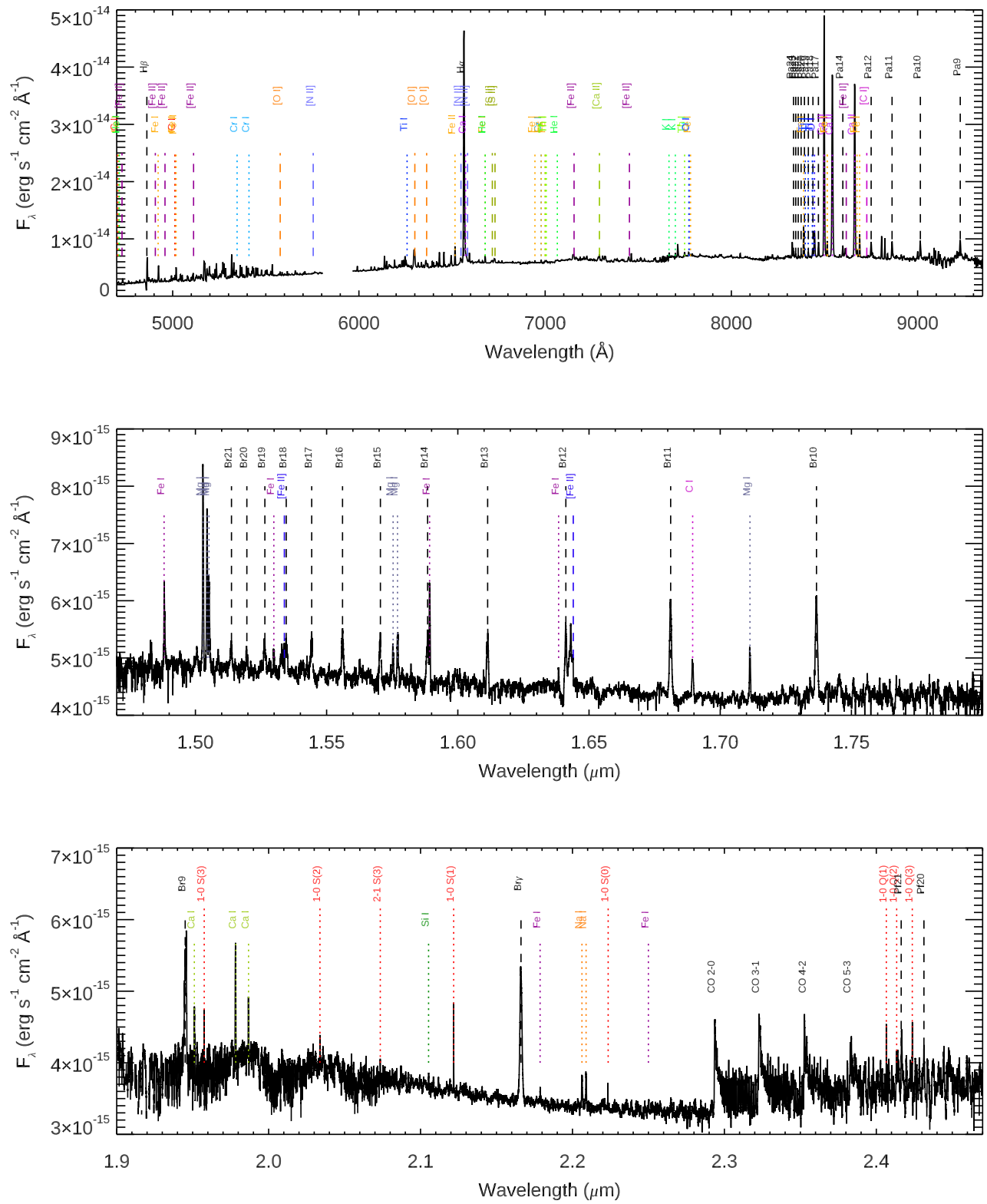


**Figure 8.** Optical (top), H (middle), and K (bottom) band spectrum of V899 Mon. Black dashed lines indicate hydrogen lines, and red dotted lines present molecular hydrogen lines. Different colors indicate different metallic species.

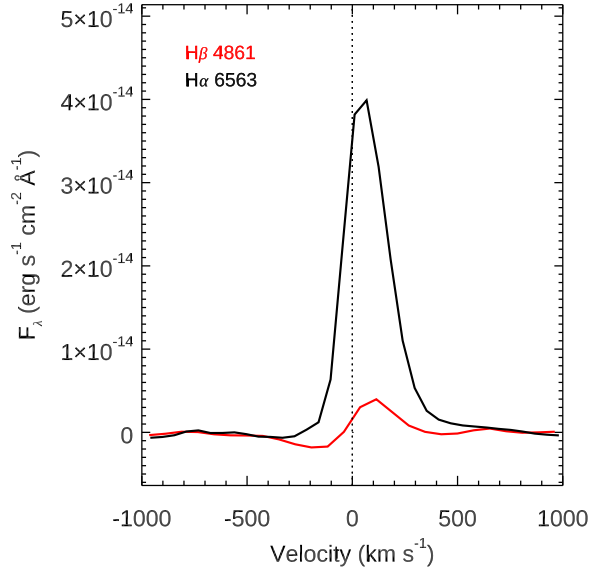


**Figure 9.** P Cygni profile of H $\beta$  4861 Å (red) and H $\alpha$  6563 Å (black).

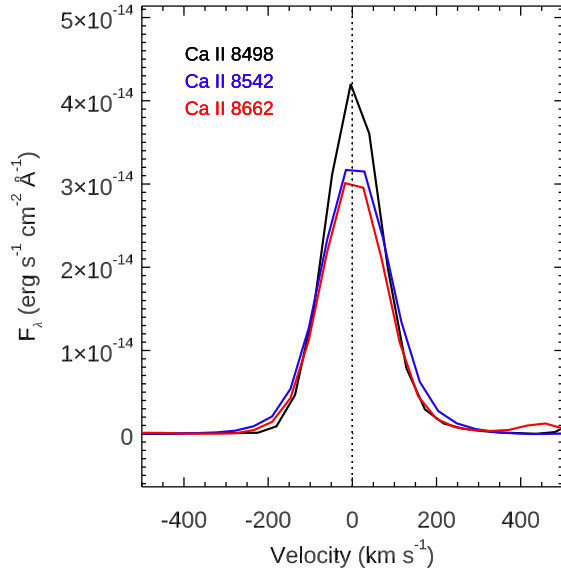


**Figure 10.** Ca II IRT emission lines: 8498 Å (black), 8542 Å (blue), and 8662 Å (red).

Hamann 1994; Hodapp et al. 2019, 2020). These lines are: [O I] 5577, 6300, 6364, [N II] 6548, [S II] 6716, 6731, [Fe II] 4728, 4907, 4959, 5112, 7155, 7453, 8617, [Ca II] 7291, [C I] 8727 Å, [Fe II] 1.533, and [Fe II] 1.644  $\mu\text{m}$ . The central peak velocity of the detected forbidden emission

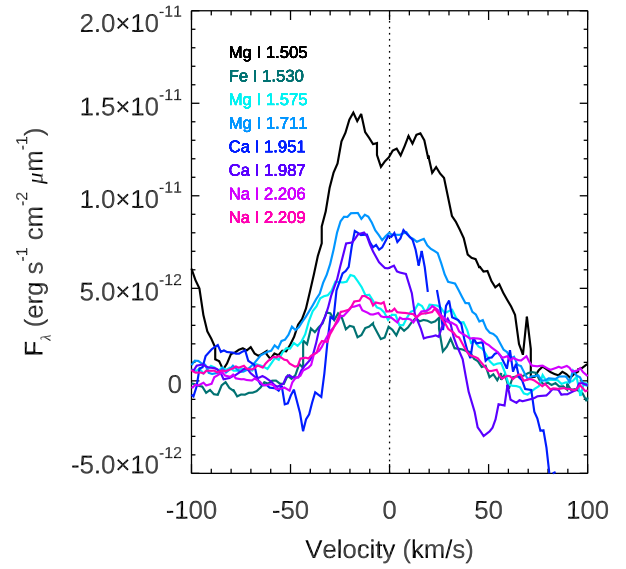


**Figure 11.** Permitted emission lines showing asymmetric double-peaked line profiles. Different colors indicate different lines.

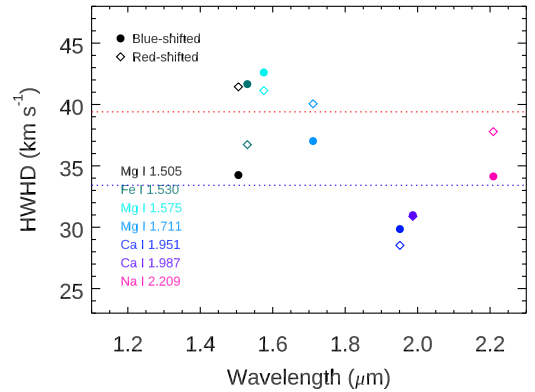


**Figure 12.** Half-width at half-depth (HWHD) as a function of wavelength. Circle and diamond symbols represent blue-shifted and red-shifted HWHD, respectively. Blue and red dotted lines show blue-shifted and red-shifted HWHD of the average permitted line profile (Figure 20). Different colors indicate different lines.

line is blue-shifted with respect to the systemic velocity by about  $-200 \text{ km s}^{-1}$ .

Forbidden emission lines in CTTS are often interpreted as jet tracers and they are typically composed of two or more velocity components (Hartigan et al. 1995). The forbidden emission lines at optical wavelengths in V899 Mon also show two components similar to CTTS (Hartigan et al. 1995; Hirth et al. 1997; Pyo et al. 2003;

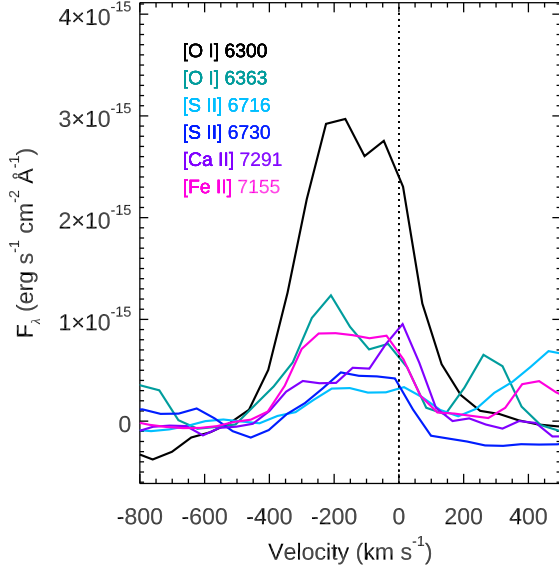


**Figure 13.** Example of strong forbidden emission lines detected in the optical spectrum. Most of the forbidden emission lines are blue-shifted about  $-200 \text{ km s}^{-1}$ .

Banzatti et al. 2019): higher velocity components between  $-400$  and  $-100 \text{ km s}^{-1}$  and relatively lower velocity components between  $-100$  and  $0 \text{ km s}^{-1}$ . Figure 13 shows examples of forbidden emission lines observed in the optical spectrum.

Figure 14 shows relatively strong forbidden emission lines in optical ([O I]  $6300 \text{ \AA}$ ) and NIR ([Fe II]  $1.644 \mu\text{m}$ ), with multiple Gaussian fittings. Higher resolution NIR [Fe II]  $1.533 \mu\text{m}$  and [Fe II]  $1.644 \mu\text{m}$  lines can be decomposed into four components around  $-340$ ,  $-275$ ,  $-175$ , and  $-35 \text{ km s}^{-1}$ . The resolved highest velocity component of the [Fe II]  $1.644 \mu\text{m}$  line is consistent with the minimum intensity of the blue-shifted absorption component ( $-332 \text{ km s}^{-1}$ ) of the H $\alpha$  P Cygni profile.

The temperature and density of the outflow region can be obtained using the forbidden emission line ratios. The electron density ( $n_e$ ) can be estimated by using three flux ratios: [S II]  $6716/6731$ , [O I]  $5577/6300$  and [Fe II]  $1.644/1.533$  (Hamann 1994; Nisini et al. 2002). The [S II]  $6716/6731$  ratio is sensitive to the density while insensitive to the temperature, and based on Figure 7 from Hamann (1994), its value (0.49) indicates the estimate  $n_e$  is higher than  $10^4 \text{ cm}^{-3}$ . The [O I]  $5577/6300$  ratio of 0.02 implies a temperature of 9000 K, and an  $n_e$  of  $10^5$ – $10^6 \text{ cm}^{-3}$ , consistent with the [S II] ratio. Finally, the  $\log([\text{Fe II}] 1.644/1.533)$  ratio, 0.40, points to  $n_e$  higher than  $10^5 \text{ cm}^{-3}$  (Figure 8 of Nisini et al. 2002), in agreement with its two previous estimations. Thus,

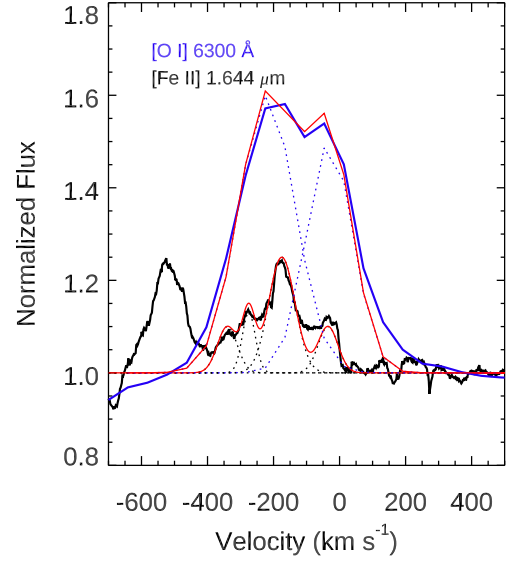


**Figure 14.** Different velocity components are detected at the [O I]  $6300 \text{ \AA}$  (blue) and [Fe II]  $1.644 \mu\text{m}$  (black) line. [O I]  $6300 \text{ \AA}$  shows two velocity components around  $-220$  and  $-30 \text{ km s}^{-1}$ , and [Fe II]  $1.644 \mu\text{m}$  shows four velocity components around  $-340$ ,  $-275$ ,  $-175$ , and  $-35 \text{ km s}^{-1}$ . Solid and dotted lines indicate the observed spectrum and each Gaussian profile. Red line presents total Gaussian profile.

the  $n_e$  of the outflow is higher than  $10^4 \text{ cm}^{-3}$ , consistent with the outbursting stage.

Electron temperature ( $T_e$ ) can be estimated by the line ratio of [Ca II]  $7291/[\text{O I}] 6300$ , [S II]  $6731/[\text{O I}] 6300$ , and [C I]  $8727/[\text{O I}] 6300$  (Figure 5 in Hamann 1994), and the obtained ratios are 0.26, 0.11, and 0.05, respectively. The [Ca II]/[O I] and [C I]/[O I] line ratios indicate  $T_e$  is below 9000 K, while the [S II]/[O I] points towards higher temperatures than this. Therefore, we assume  $T_e$  must be around 9000 K. The obtained temperature is similar to that of the outbursting stage (9000 K; Nisini et al. 2015), which suggests the outflow temperature and density of V899 Mon might not be directly affected by the accretion process.

### 3.2.5. Mass accretion rates

Several atomic emission lines formed by the accretion process are found in the optical and NIR spectrum. In order to estimate the mass accretion rate, the interstellar extinction of  $A_V=2.6$  (Nisini et al. 2015) was corrected by adopting the extinction curve of Cardelli et al. (1989).

The line flux ( $F_{\text{line}}$ ) of emission lines was measured by fitting a Gaussian with a Monte Carlo method. The line flux of each line was measured 100 times with random Gaussian errors multiplied by the observation er-

rors. The standard deviation derived from all 100 measurements was adopted as the uncertainty of line flux. The measured line fluxes and uncertainties are listed in Table 2. Then, the line luminosity ( $L_{\text{line}}$ ), accretion luminosity ( $L_{\text{acc}}$ ), and mass accretion rate ( $\dot{M}_{\text{acc}}$ ) are estimated by the following Eqs. 1–3. Accretion luminosity was calculated by adopting the coefficients of Alcalá et al. (2017) for a and b in Eq. 2.

$$L_{\text{line}} = 4\pi d^2 \cdot F_{\text{line}} \quad (1)$$

$$\log\left(\frac{L_{\text{acc}}}{L_{\odot}}\right) = a \cdot \log\left(\frac{L_{\text{line}}}{L_{\odot}}\right) + b \quad (2)$$

$$\dot{M}_{\text{acc}} = \left(1 - \frac{R_*}{R_{\text{in}}}\right)^{-1} \frac{L_{\text{acc}} R_*}{GM_*} \approx 1.25 \frac{L_{\text{acc}} R_*}{GM_*}, \quad (3)$$

where  $R_{\text{in}}$  is the disk inner radius and assumed to be  $5R_*$  (Gullbring et al. 1998).

In order to compare  $\dot{M}_{\text{acc}}$  in our observations with those of the outbursting phase, we adopted the same distance (905 pc), stellar mass ( $2.5 M_{\odot}$ ), and stellar radius ( $4 R_{\odot}$ ) as Ninan et al. (2015) assumed. The calculated  $\dot{M}_{\text{acc}}$  is listed in Table 2. The  $\dot{M}_{\text{acc}}$  estimated in our observations are in the range of  $6.0 \times 10^{-8}$  to  $4.8 \times 10^{-7} M_{\odot} \text{ yr}^{-1}$ , which are about an order of magnitude lower than those of the outbursting phase (see Figure 15 in Ninan et al. 2015). The mean and standard deviation of  $\dot{M}_{\text{acc}}$  is  $(2.2 \pm 1.3) \times 10^{-7} M_{\odot} \text{ yr}^{-1}$ . If we use the  $2M_{\odot}$  obtained from our disk model (see Section 3.2.9), the calculated  $\dot{M}_{\text{acc}}$  is between  $7.4 \times 10^{-8}$  to  $6.0 \times 10^{-7} M_{\odot} \text{ yr}^{-1}$ . The mean and standard deviation of  $\dot{M}_{\text{acc}}$  is  $(2.7 \pm 1.6) \times 10^{-7} M_{\odot} \text{ yr}^{-1}$ , which are in agreement with those of  $\dot{M}_{\text{acc}}$  obtained with  $2.5 M_{\odot}$  within the standard deviation. The  $\dot{M}_{\text{acc}}$  of V899 Mon is lower than FUors (Audard et al. 2014, and references therein) but similar to EX Lup during its outburst ( $(2 \pm 0.5) \times 10^{-7} M_{\odot} \text{ yr}^{-1}$ ; Aspin et al. 2010).

### 3.2.6. Mass loss rates

Mass loss rate was estimated by using the relation of  $\log \dot{M} = -8.6 + 0.7 \log L_{\text{bol}}$  (Nisini et al. 1995).  $L_{\text{bol}}$  of  $21 L_{\odot}$  is used for this relation that is obtained from the SED of our observations. The calculated mass loss rate is about  $2.1 \times 10^{-8} M_{\odot} \text{ yr}^{-1}$ , which is about one order of magnitude lower than that of the outbursting phase ( $1 \times 10^{-7} M_{\odot} \text{ yr}^{-1}$ ; Ninan et al. 2015). The estimated mass loss rate is lower than those of FUors, while similar to those of CTTS (Hartmann & Kenyon 1996, and references therein). In addition, the estimated mass loss rate is about 10% of the mass accretion rate, which is consistent with those of CTTS (Hartmann &

Kenyon 1996; Hartmann 2009; Ellerbroek et al. 2013; Bally 2016).

### 3.2.7. Molecular Hydrogen Lines

$\text{H}_2$  emission lines are known as tracers of outflows in young stars (Davis et al. 2003, 2010, 2011; Bally et al. 2007; Greene et al. 2010; Bally 2016; Nisini et al. 2002; van den Ancker et al. 1999; Fernandes 2000). Several  $\text{H}_2$  rovibrational transitions were detected in our observation (red dotted lines in Figure 8), which is not common either in FUors or in EXors. Only V346 Nor (Kóspál et al. 2020) shows several  $\text{H}_2$  emission lines similar to V899 Mon. The  $\text{H}_2$  2.122  $\mu\text{m}$  emission line was detected in the FUor V960 Mon (Park et al. 2020) and in some EXors (Kóspál et al. 2011a; Hodapp et al. 2019, 2020), however, none of the other  $\text{H}_2$  transitions were detected.

The excitation diagram of  $\text{H}_2$  lines (Figure 15) is used to estimate the gas excitation temperature ( $T_{\text{ex}}$ ) and the column density ( $N_{\text{H}_2}$ ) (van den Ancker et al. 1999; Fernandes 2000; Nisini et al. 2002; Davis et al. 2011). The column density ( $N_{v,J}$ ) was obtained using dereddened ( $A_V=2.6$ ) line intensity ( $I_{v,J}$ ), transition probability ( $A_{v,J}$ ; Turner et al. 1977), and wavelength ( $\lambda$ ) in micron (Eq. 4).

$$N_{v,J} = \frac{4\pi\lambda I_{v,J}}{hcA_{v,J}} \quad (4)$$

The column density ( $N_{v,J}$ ) is proportional to the statistical weight ( $g_{v,J}$ ) and upper energy level ( $E_{v,J}$ ) temperature by assuming thermodynamic equilibrium.

$$N_{v,J} = g_{v,J} \exp\left(\frac{E_{v,J}}{kT_{\text{ex}}}\right) \quad (5)$$

If the gas is thermalized, the excitation diagram will be fitted by a single straight line. The  $T_{\text{ex}}$  can be obtained from the inverse slope of the line, and the  $N_{v,J}$  can be estimated from the y-intercept. The resulting  $T_{\text{ex}}$  and  $N_{\text{H}_2}$  are  $2528 \pm 1436$  K and  $4.5 \pm 3.6 \times 10^6 \text{ cm}^{-2}$ , respectively. The measured  $T_{\text{ex}}$  agrees well with V346 Nor ( $T_{\text{ex}} = 2100 \pm 100$  K; Kóspál et al. 2020) within the uncertainty and is similar to the  $T_{\text{ex}}$  (2000–3000 K) of Class I or Class II, which is known to be caused by other shock-heated gases (Beck et al. 2008; Davis et al. 2011).

The intensity ratio of 1-0/2-1 S(1) is generally used for studying the shock mechanism. In our observation, only 1-0 S(1) line is detected, so we used the ratio of 1-0/2-1 S(3), which shows equivalent but better results than S(1) lines (Smith 1995). We determine a ratio value of 2.3, which is closer to the ratio of 4, indicative of J-shock, rather than a value of 20, indicative of cool-C shock (Smith 1995).

**Table 2.** Line Information

Transition	Wavelength (Å)	$F_{\text{line}}$ (Obs.) (erg s <sup>-1</sup> cm <sup>-2</sup> )	$F_{\text{line}}$ ( $A_V$ Corr.) (erg s <sup>-1</sup> cm <sup>-2</sup> )	$L_{\text{line}}$ ( $L_{\odot}$ )	$L_{\text{acc}}$ ( $L_{\odot}$ )	$M_{\text{acc}}$ ( $M_{\odot}$ yr <sup>-1</sup> )
H $\beta$	4861.33	1.19E-14 $\pm$ 1.39E-15	1.97E-13 $\pm$ 7.56E-14	5.02E-03	9.31E-01	5.95E-08
Fe I	4921.93	9.15E-15 $\pm$ 1.18E-15	1.57E-13 $\pm$ 2.16E-14	4.00E-03	5.68E+00	3.63E-07
He I	5015.68	3.73E-15 $\pm$ 1.03E-15	5.51E-14 $\pm$ 1.41E-14	1.40E-03	4.63E+00	2.96E-07
H $\alpha$	6562.80	2.17E-13 $\pm$ 1.07E-14	1.54E-12 $\pm$ 7.01E-14	3.92E-02	1.42E+00	9.05E-08
He I	6678.15	3.92E-15 $\pm$ 1.61E-15	2.58E-14 $\pm$ 1.10E-14	6.58E-04	5.28E+00	3.37E-07
He I	7065.19	1.26E-15 $\pm$ 1.74E-15	8.38E-15 $\pm$ 9.99E-15	2.14E-04	1.38E+00	8.80E-08
O I	7773.05	2.32E-15 $\pm$ 1.90E-15	1.07E-14 $\pm$ 7.90E-15	2.73E-04	1.36E+00	8.69E-08
Ca II	8498.02	2.00E-13 $\pm$ 9.75E-15	7.13E-13 $\pm$ 3.46E-14	1.82E-02	7.53E+00	4.81E-07
Ca II	8542.09	1.92E-13 $\pm$ 1.00E-14	6.75E-13 $\pm$ 3.46E-14	1.72E-02	5.23E+00	3.34E-07
Ca II	8662.14	1.71E-13 $\pm$ 9.23E-15	5.83E-13 $\pm$ 3.14E-14	1.49E-02	3.98E+00	2.54E-07
O I	8446.36	2.11E-14 $\pm$ 2.97E-15	7.81E-14 $\pm$ 1.17E-14	1.99E-03	3.49E+00	2.23E-07
Pa10	9014.91	1.52E-14 $\pm$ 2.55E-15	4.70E-14 $\pm$ 8.59E-15	1.20E-03	1.74E+00	1.11E-07
Pa9	9229.01	1.53E-14 $\pm$ 2.71E-15	4.67E-14 $\pm$ 8.60E-15	1.19E-03	1.82E+00	1.16E-07
Br $\gamma$	21661.21	3.11E-14 $\pm$ 2.95E-16	4.12E-14 $\pm$ 2.90E-16	1.05E-03	2.99E+00	1.91E-07
Fe II	4958.82	1.87E-15 $\pm$ 7.12E-16	2.95E-14 $\pm$ 1.24E-14	...	...	...
[O I]	5577.34	6.22E-16 $\pm$ 1.18E-15	5.55E-15 $\pm$ 1.31E-14	...	...	...
[O I]	6300.30	2.52E-14 $\pm$ 2.68E-15	1.97E-13 $\pm$ 2.16E-14	...	...	...
[O I]	6363.78	8.38E-15 $\pm$ 2.17E-15	6.58E-14 $\pm$ 1.69E-14	...	...	...
Fe II	6516.08	1.08E-14 $\pm$ 1.79E-15	8.50E-14 $\pm$ 1.55E-14	...	...	...
[N II]	6548.05	5.74E-15 $\pm$ 2.43E-15	4.20E-14 $\pm$ 1.68E-14	...	...	...
[S II]	6716.44	2.86E-15 $\pm$ 2.29E-15	1.97E-14 $\pm$ 1.55E-14	...	...	...
[S II]	6730.82	5.85E-15 $\pm$ 2.42E-15	4.34E-14 $\pm$ 1.64E-14	...	...	...
[Fe II]	7155.17	7.74E-15 $\pm$ 2.48E-15	4.59E-14 $\pm$ 1.45E-14	...	...	...
[Ca II]	7291.47	6.64E-15 $\pm$ 2.64E-15	3.42E-14 $\pm$ 1.66E-14	...	...	...
K I	7664.90	2.36E-15 $\pm$ 1.77E-15	1.16E-14 $\pm$ 7.13E-15	...	...	...
K I	7698.96	1.41E-15 $\pm$ 1.54E-15	6.35E-15 $\pm$ 6.29E-15	...	...	...
[C I]	8727.13	1.19E-15 $\pm$ 1.83E-15	3.51E-15 $\pm$ 6.12E-15	...	...	...
Fe I	8387.77	1.52E-14 $\pm$ 2.14E-15	6.65E-14 $\pm$ 1.19E-14	...	...	...
Transition	Wavelength ( $\mu\text{m}$ )	Line Flux (Obs.) (erg s <sup>-1</sup> cm <sup>-2</sup> )	Line Flux ( $A_V$ Corr.) (erg s <sup>-1</sup> cm <sup>-2</sup> )			
Br21	1.5137	3.47E-15 $\pm$ 1.87E-16	5.60E-15 $\pm$ 2.02E-16	...	...	...
Br20	1.5196	2.23E-15 $\pm$ 1.81E-16	3.63E-15 $\pm$ 1.83E-16	...	...	...
Br19	1.5265	5.14E-15 $\pm$ 5.05E-16	8.41E-15 $\pm$ 4.11E-16	...	...	...
Br17	1.5443	4.99E-15 $\pm$ 1.95E-16	8.12E-15 $\pm$ 2.03E-16	...	...	...
Br16	1.5561	5.75E-15 $\pm$ 1.89E-16	9.20E-15 $\pm$ 1.86E-16	...	...	...
Br15	1.5705	4.55E-15 $\pm$ 2.34E-16	7.15E-15 $\pm$ 2.04E-16	...	...	...
Br13	1.6114	6.46E-15 $\pm$ 2.14E-16	1.02E-14 $\pm$ 2.10E-16	...	...	...
Br12	1.6412	7.68E-15 $\pm$ 2.97E-15	1.19E-14 $\pm$ 2.27E-15	...	...	...
Br11	1.6811	1.45E-14 $\pm$ 1.79E-16	2.19E-14 $\pm$ 2.09E-16	...	...	...
Br10	1.7367	1.69E-14 $\pm$ 2.26E-16	2.52E-14 $\pm$ 2.09E-16	...	...	...
Br9	1.9451	2.44E-14 $\pm$ 2.90E-16	3.39E-14 $\pm$ 2.52E-16	...	...	...
Pf21	2.4164	5.86E-15 $\pm$ 1.95E-16	7.43E-15 $\pm$ 1.95E-16	...	...	...
Pf20	2.4314	3.29E-15 $\pm$ 1.74E-16	4.15E-15 $\pm$ 1.81E-16	...	...	...
1-OS(3)	1.9580	1.10E-15 $\pm$ 8.65E-17	1.52E-15 $\pm$ 8.78E-17	...	...	...
1-OS(2)	2.0340	6.26E-16 $\pm$ 8.64E-17	8.48E-16 $\pm$ 9.72E-17	...	...	...
2-1S(3)	2.0730	4.88E-16 $\pm$ 8.44E-17	6.64E-16 $\pm$ 7.71E-17	...	...	...
1-OS(1)	2.1220	1.66E-15 $\pm$ 9.24E-17	2.21E-15 $\pm$ 8.65E-17	...	...	...
1-OS(0)	2.2230	5.43E-16 $\pm$ 1.15E-16	7.10E-16 $\pm$ 9.85E-17	...	...	...
1-0Q(1)	2.4070	8.97E-16 $\pm$ 6.92E-17	1.13E-15 $\pm$ 6.88E-17	...	...	...
1-0Q(3)	2.4240	1.75E-15 $\pm$ 2.68E-16	2.20E-15 $\pm$ 2.94E-16	...	...	...

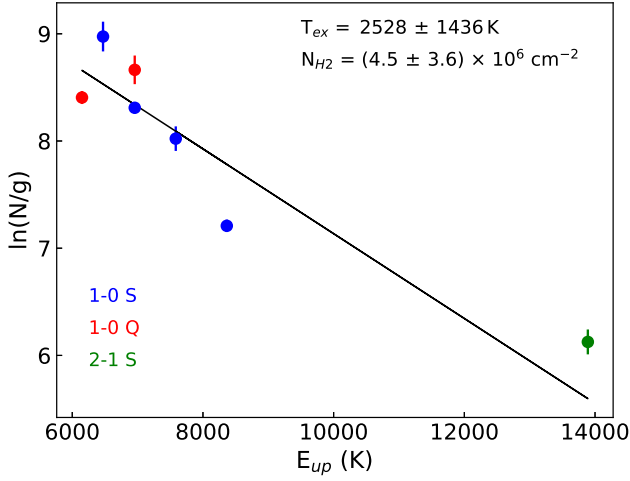


**Figure 15.** Excitational diagram of  $H_2$ .

### 3.2.8. Hydrogen lines

During the second outburst stage, several Balmer series lines were observed ( $H\alpha$  to  $H8$ ; Ninan et al. 2015) as P Cygni, emission, or absorption profiles. However, our observations revealed only two Balmer lines ( $H\alpha$  and  $H\beta$ ) to have the P Cygni profile. In addition, we detected several Paschen series (Pa 9 to Pa 24) in emission. These line profiles are shown in Figure 24 in Appendix C.

The  $Br\gamma$  2.166  $\mu\text{m}$  line was not detected by Ninan et al. (2015) during the second outburst observation period, consistent with the characteristics of FUors (Connelley & Reipurth 2018). On the other hand, during our observations, Brackett series lines from Br 7 to Br 21 and two Pfund series lines (Pf 20 and Pf 21) are observed in emission. Relatively strong Br lines are presented in Figure 16, and all the detected Br and Pf lines are presented in Appendix C (Figure 25). The detection of these Hydrogen emission lines is similar to EXors or CTTS (Aspin 2011; Kóspál et al. 2011a; Hodapp et al. 2019, 2020).

In order to estimate the physical conditions of the emitting region, we used the excitation diagram of the Br series in Figure 17. The observed line fluxes with respect to the  $Br\gamma$  were compared with the Case B theory (Hummer & Storey 1987). Case B theory assumes that the Lyman lines are optically thick and other lines are optically thin. The best fit model (red line) is for an electron temperature ( $T_e$ ) of 5,000 K and an electron density ( $N_e$ ) of  $10^9 \text{ cm}^{-3}$ . The best fit  $T_e$  is lower than that of the outbursting stage of EX Lup ( $T_e=10,000 \text{ K}$ ), while  $N_e$  is higher than EX Lup ( $N_e=10^7 \text{ cm}^{-3}$ ; Kóspál et al. 2011a). The lower temperature and higher density

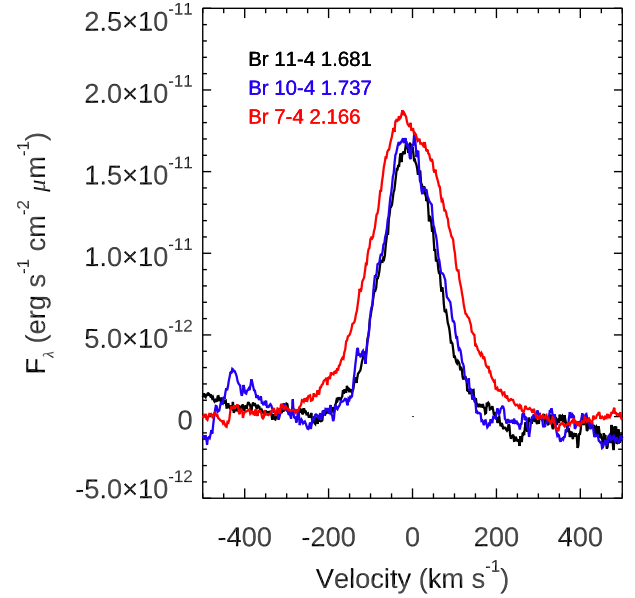


**Figure 16.** Relatively strong and clear Br series are presented: Br11 1.681  $\mu\text{m}$  (black), Br10 1.731  $\mu\text{m}$  (blue), and  $Br\gamma$  2.166  $\mu\text{m}$  (red).

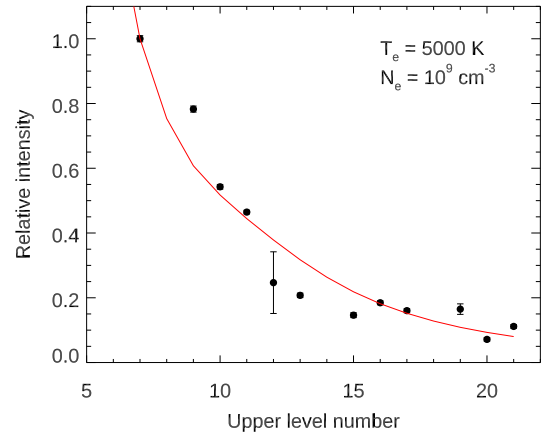


**Figure 17.** Excitation diagram of Brackett series. Black symbol indicates observed line flux divided by  $Br\gamma$  2.166  $\mu\text{m}$ . Red solid line presents the Case B theory of  $T_e = 5000 \text{ K}$  and  $N_e = 10^9 \text{ cm}^{-3}$  (Hummer & Storey 1987).

than the EX Lup in the outbursting stage are may be because V899 Mon is in the fading stage.

### 3.2.9. Disk modeling of the CO and metallic features

In order to study the CO bandhead emission features, we normalized the  $K$  band spectrum by fitting a fifth order polynomial to the 2.10–2.29  $\mu\text{m}$  and 2.40–2.47  $\mu\text{m}$



wavelength ranges using a robust fitting method and divided the spectrum by this polynomial. The resulting spectrum is plotted with black in Figure 18. The spectral resolution of IGRINS is high enough to resolve some of the individual rovibrational lines that make up the CO bandhead. To obtain a high signal-to-noise ratio line profile, we averaged 14 R-branch lines from  $J = 14 - 15$  to  $J = 27 - 28$  for  $v = 2 - 0$  and 10 R-branch lines from  $J = 13 - 14$  to  $J = 22 - 23$  for  $v = 3 - 1$  after each line was normalized again by its peak value. These profiles can be seen in Figure 19. Both the  $v = 2 - 0$  and the  $v = 3 - 1$  profile show clear Keplerian double-peaked shape, but both are clearly asymmetric. The asymmetry is different from what is observed for the atomic lines. The atomic lines were broader towards the red and narrower towards the blue, while the CO profile is symmetric for velocities  $|v| > 25 \text{ km s}^{-1}$ , and the asymmetry is only visible for the Keplerian peaks at  $|v| < 25 \text{ km s}^{-1}$ .

To derive the geometrical parameters of the disk and the dynamical stellar mass, we calculated a simple disk model with inner and outer radii of  $R_{\text{in}}$  and  $R_{\text{out}}$ , inclination of  $i$ , in Keplerian rotation around a star with a mass  $M_*$ , and having a power law brightness distribution with an exponent  $\alpha$ . We calculated the radial velocity for each point in the disk and shifted a Gaussian that corresponds to the finite instrumental spectral resolution of IGRINS (45,000) by this velocity. Then we computed the full disk's spectrum by integrating over the whole disk in each spectral channel. We considered  $R_{\text{in}}$  from 0.10 au to 0.75 au, with 0.05 au increments,  $R_{\text{out}}$  from 2.5 au to 5.5 au, with 0.5 au increments,  $i$  from  $41^\circ$  to  $59^\circ$  with  $3^\circ$  increments,  $M_*$  from  $1.7 M_\odot$  to  $2.3 M_\odot$  with  $0.1 M_\odot$  increments, and a power law exponent of the brightness profile,  $\alpha$  from  $-1.85$  to  $-2.15$  in 0.05 increments. This resulted in grid of  $14 \times 7 \times 7 \times 7 \times 7 = 33614$  models.

We compared the observed line profile with the models by calculating the  $\chi^2$  taking into account only the blue-shifted channels between  $-50 \text{ km s}^{-1} < v < 0 \text{ km s}^{-1}$ . We determined the best-fitting model parameters and their uncertainties by marginalizing in each parameter. We found that the results are not sensitive to the variation of the  $\alpha$  parameter, so this was eventually fixed to  $-2$ . The best fitting parameters are listed in Table 3. The parameters we obtained for the  $v = 2 - 0$  profile and for the  $v = 3 - 1$  profile are identical within the uncertainties, although there is a  $1\sigma$  hint that the outer radius is smaller for the  $v = 3 - 1$  lines than for the  $v = 2 - 0$  lines (3.6 au vs. 4.2 au). This is understandable if we consider that the  $v = 3 - 1$  lines are higher excitation lines, therefore there should be outer disk regions (be-

tween 3.6 au and 4.2 au) where they are not excited any more, while the lower excitation  $v = 2 - 0$  lines are still excited. In Figure 19, we plotted the model line profile that uses the average of the parameters obtained from the  $v = 2 - 0$  and  $v = 3 - 1$  fits. These parameters are also indicated in Table 3.

To derive physical parameters such as the column density ( $N_{\text{CO}}$ ) and excitation temperature ( $T_{\text{ex}}$ ) of the CO gas that emits the bandhead feature, we modeled the CO lines of V899 Mon following our earlier approach in Kóspál et al. (2011a) for EX Lup. We used Eq. 10 from Kraus et al. (2000) to calculate the absorption coefficient  $\kappa$  of the CO molecules. We approximated the thermal and turbulent broadening using a simple Gaussian. We multiplied  $\kappa$  with the  $N_{\text{CO}}$  to obtain the optical depth  $\tau$ . We assumed a simple slab, so that the  $N_{\text{CO}}$  and  $T_{\text{ex}}$  of the CO gas were identical everywhere in the disk. We calculated the intensity  $I$  following:

$$I = BB(T_{\text{ex}})(1 - e^{-\tau/\cos(i)}), \quad (6)$$

where  $BB(T_{\text{ex}})$  is the Planck function corresponding to the  $T_{\text{ex}}$ . We convolved the model spectrum with the disk's velocity profile determined in the previous step. We varied  $T_{\text{ex}}$  between 1500 K and 6400 K, in steps of 50 K, and  $N_{\text{CO}}$  between  $10^{19} \text{ cm}^{-2}$  and  $10^{24} \text{ cm}^{-2}$  in logarithmic scale, in steps of 0.05 in the exponent. We used this model spectrum and the observed spectrum in Figure 18 to calculate  $\chi^2$ , and after marginalization, obtained the following parameters:  $T_{\text{ex}} = 2482 \pm 326 \text{ K}$  and  $N_{\text{CO}} = 10^{(22.18 \pm 0.30)} \text{ cm}^{-2}$ . The best fitting model is plotted with red in Figure 18. In order to check the underestimated  $v = 2 - 0$  bandhead part, we also modeled only for the  $v = 2 - 0$ . As a result, we obtained a similar temperature ( $T_{\text{ex}} = 2417 \pm 377 \text{ K}$ ) and column density ( $N_{\text{CO}} = 10^{(22.59 \pm 0.37)} \text{ cm}^{-2}$ ) within the uncertainty. A similar temperature of best-fit results from the whole and only  $v = 2 - 0$  bandhead part suggests that the disk is thermalized (Lee et al. 2015).

Figure 11 clearly shows that the atomic metal line profiles show the double-peaked Keplerian rotation. We may therefore assume that these lines are also emitted in a disk, just like the CO lines. Previously, we determined geometrical disk parameters, and in particular, we constrained the region of the disk that emits the CO bandhead feature in the K band. Here, we use the same disk model to find out the disk region that emits the metallic lines. Because the metallic lines are noisier than the CO line profile we obtained by averaging several R-branch lines, we did not attempt to fit the metallic lines separately, but we normalized them to their peak values and averaged them. This average metallic line profile is plotted in Figure 20. This shows that not only the Kep-

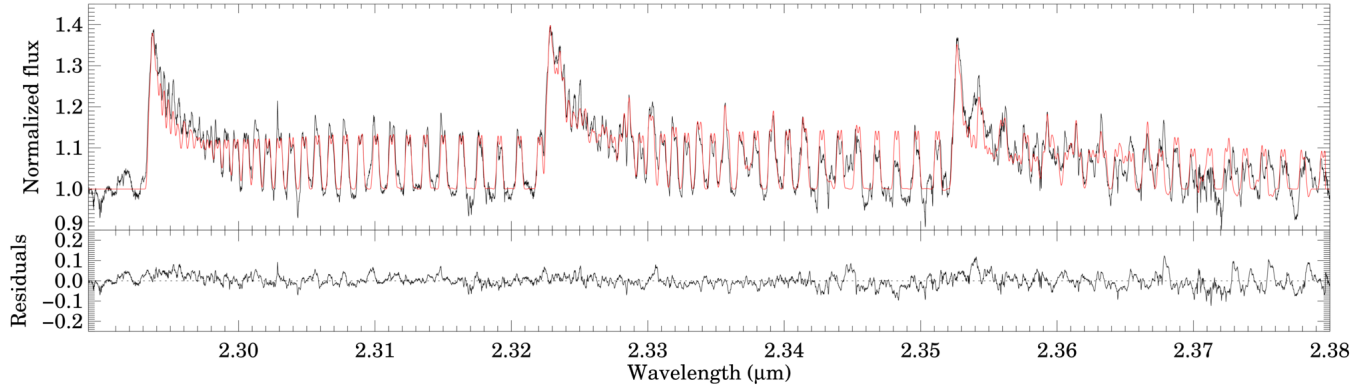


**Figure 18.** In the top panel with the black line, we show the CO overtone bandhead emission in the spectrum of V899 Mon. The best-fitting model with  $T_{\text{ex}} = 2482$  K and  $N_{\text{CO}} = 10^{22.18} \text{ cm}^{-2}$  is plotted in red, while the lower panel shows the residuals.

**Table 3.** Disk parameters and dynamical stellar mass for V899 Mon.

Parameter	CO $v = 2 - 0$	CO $v = 3 - 1$	Average CO	Atomic (blue-shifted)	Atomic (red-shifted)
$i$ ( $^\circ$ )	$51.01 \pm 10.82$	$52.54 \pm 9.61$	$51.77 \pm 10.22$	51.77 (fixed)	51.77 (fixed)
$R_{\text{in}}$ (au)	$0.55 \pm 0.20$	$0.62 \pm 0.16$	$0.58 \pm 0.18$	$0.41 \pm 0.28$	$0.20 \pm 0.15$
$R_{\text{out}}$ (au)	$4.17 \pm 1.34$	$3.55 \pm 1.04$	$3.86 \pm 1.19$	$4.46 \pm 1.94$	$3.73 \pm 1.86$
$M_*$ ( $M_\odot$ )	$2.00 \pm 0.67$	$2.08 \pm 0.57$	$2.04 \pm 0.42$	2.04 (fixed)	2.04 (fixed)
$\alpha$	-2.00 (fixed)	-2.00 (fixed)	-2.00 (fixed)	-2.00 (fixed)	-2.00 (fixed)

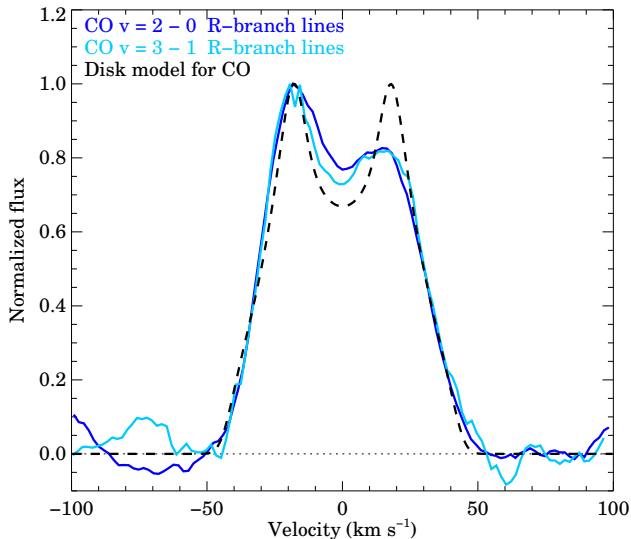


**Figure 19.** Average line profiles of the  $v = 2 - 0$  and  $v = 3 - 1$  rovibrational lines of V899 Mon. The disk model that fits the blue-shifted side of the line profiles is indicated with the dashed curve. The corresponding model parameters are in Table 3.

lerian peaks are asymmetric, but also the line is broader in the red side and narrower in the blue side. Therefore, we fitted the blue-shifted ( $-60 \text{ km s}^{-1} < v < 0 \text{ km s}^{-1}$ ) and red-shifted ( $0 \text{ km s}^{-1} < v < 80 \text{ km s}^{-1}$ ) sides of the

profile separately. Because of the lower signal-to-noise ratio, we decided to fix not only the power law exponent of the brightness profile, but also the disk inclination and stellar mass. Therefore, the only free parameters were the inner and outer disk radii. The best-fitting parameters can be found in Table 3.

Our results show that for the blue-shifted side, the emitting region of the metallic lines extends closer to the star than that of CO (0.41 au instead of 0.58 au), and it is also more extended outwards (4.46 au instead of 3.86 au). The smaller inner radius is apparent because the metallic line profile is broader than the CO line profile, while the larger outer radius is visible in the velocity channels around 0, where the metallic lines only show a small dip, while the CO profile has a deep dip between the two maxima. For the red-shifted side, which is even broader, we obtained an even smaller inner radius, 0.20 au. This suggests that there is a significant asymmetry in the disk: on the red-shifted side, the hot gas (traced by the metals) extends much closer to the star than on the blue-shifted side. The CO profile does not show such an asymmetry, which is understandable if we consider that it traces cooler gas than the metals; there is not much CO emission inside of 0.6 au, while the fit results for the metallic line profile suggest that the asymmetry happens somewhere between 0.2 and 0.4 au.

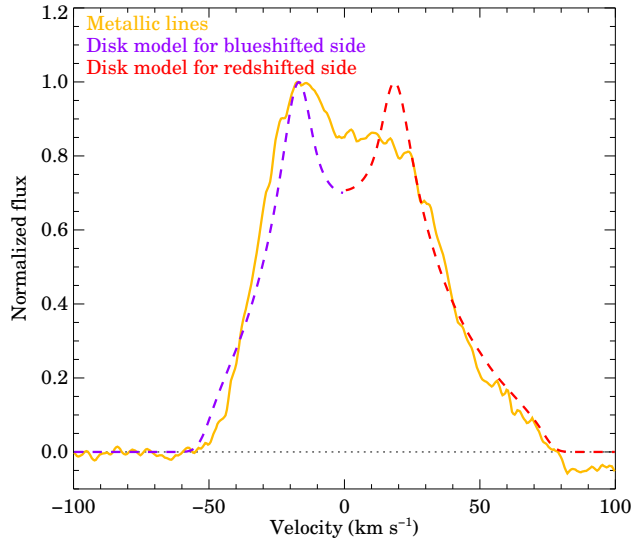


**Figure 20.** Average line profile of various atomic lines of V899 Mon. Two different disk models that fit the blue-shifted and red-shifted sides of the line profile are indicated with the dashed curves.

### 3.2.10. Spectro-astrometry

We took advantage of MUSE’s sensitivity and resolution to carry out a spectro-astrometric analysis of our target. The presence of extended emission moving at different velocities with respect to the star would slightly shift the position of the star in each channel with respect to the continuum. We began by fitting a 2D Gaussian to the position of the star in each channel of the data cube. Then for each line identified in the spectrum (top panel of Figure 8) we selected a velocity window of a few hundreds of  $\text{km s}^{-1}$  and calculated the median (i.e. the position of the continuum). Finally, for each channel in the velocity window, we calculated the difference between the best fitted position and the median.

In Figure 21 we show the results of four lines: [O I] 6300 Å, H $\alpha$  6563 Å, O I 8446 Å, and Ca II 8498 Å. The top row panels show the spectral line, the middle rows show the absolute differences in position, and the bottom panels show the position of the emission per channel relative to the center of the continuum. In the case of the absolute difference of position, if the emission line traces infalling or outflowing material the absolute differences in position would be positive or negative, respectively. However, if the line is tracing disk rotation then the differences would be positive on one side and negative on the other. In the case of the relative positions, the infalling or outflowing material should be separated from the position of the star in one direction, and the disk rotation would be detected on opposite positions with

respect to the star, thus indicating which side of the disk is blue-shifted or red-shifted.

Based on the middle row of Figure 21, [O I] 6300 Å and H $\alpha$  6563 Å show outflow emission, and O I 8446 Å and Ca II 8498 Å show disk rotation. The former two lines show the blue-shifted emission extends towards the bottom left quadrant, i.e. the southeast of V899 Mon. The latter two lines show blue-shifted and red-shifted disk emission in the upper left and lower right quadrants, respectively, indicating the disk has a Northeast-Southwest orientation. We fitted a straight line to these points of extended emission, and found the [O I] 6300 Å and H $\alpha$  6563 Å outflow emission have position angles of  $\sim 140^\circ$  and  $\sim 130^\circ$ , respectively, and the point of O I 8446 Å and Ca II 8498 Å have position angles of  $\sim 55^\circ$  and  $\sim 58^\circ$ , respectively. The disk position angles are within the uncertainties of those estimated from ALMA dust continuum observations (Kóspál et al. 2021), and are almost perpendicular ( $\sim 80^\circ$ ) to those of the high-velocity outflow emission. Spectro-astrometry of the O I 8446 Å and Ca II 8498 Å lines (bottom panels in Figure 21) shows consistent results with permitted metallic lines with the disk size from 0.2 to 4.6 au (Table 3).

The blue-shifted emission of [O I] 6300 Å shows two peaks, at  $-24 \text{ km s}^{-1}$  and  $-175 \text{ km s}^{-1}$ , indicative of a combination of low-velocity and high-velocity components, respectively, as has been detected on several T Tauri stars (e.g. Hartigan et al. 1995; Hirth et al. 1997; Pyo et al. 2003; Banzatti et al. 2019). The blue-shifted components of [O I] 6300 Å and H $\alpha$  6563 Å reach maximum velocities of  $-500 \text{ km s}^{-1}$ . We estimated the ejection dates for the outflows using an average outflow velocity of  $250 \text{ km s}^{-1}$ , and the outflow separations are 10 au for [O I] 6300 Å and 40 au for H $\alpha$  6563 Å (see bottom panels of Figure 21). The deprojected outflow velocity, assuming an average system inclination of  $50^\circ$  (see Table 1), is  $385 \text{ km s}^{-1}$ . Thus, under the assumption that outflow velocity remains constant after its ejection, we estimate ejection timelines of 45 and 180 days for [O I] 6300 Å and H $\alpha$  6563 Å, respectively. However, these time estimates must be taken with caution as the uncertainties in the astrometry and the spectral resolution of MUSE, and the large uncertainties in the disk inclination, can change this timelines by a factor of a few. Nevertheless, the tentative estimated ejection date for [O I] 6300 Å is early December 2020, which is in agreement with the 2020/2021 accretion burst (red symbols in Figure 3). And the estimated ejection date for H $\alpha$  6563 Å is late July 2020, which falls during a period when the photometric monitoring of V899 Mon is sparse. We suggest this difference in time estimates can be partially explained by the different physical phenom-

ena each line traces. Both [O I] 6300 Å and H $\alpha$  6563 Å trace outflow emission, however, the latter also traces accretion in the inner parts of the circumstellar disk.

#### 4. DISCUSSION

##### 4.1. Current status of V899 Mon

The small-amplitude brightness variations observed in V899 Mon in recent years is common for CTTS. The accretion bursts that started to occur since 2016 (including the two unique, particularly well-characterized bursts marked by red symbols in Figure 3) appear to be caused by the magnetospheric accretion process, similarly as in CTTS. The rich emission spectrum of V899 Mon is also similar to those of CTTS: hydrogen, permitted, and forbidden metallic emission lines (Muzerolle et al. 1998). Calculated mass accretion rate and mass loss rate are about  $10^{-7} M_{\odot} \text{ yr}^{-1}$  and  $10^{-8} M_{\odot} \text{ yr}^{-1}$ , respectively. These values are lower than those of FUors but similar to those of CTTS (Muzerolle et al. 1998), and the mass loss rate is about 10% of the mass accretion rate that is also in agreement with CTTS (Hartmann & Kenyon 1996; Hartmann 2009; Ellerbroek et al. 2013; Bally 2016). The intensity ratio of the Ca II IRT lines is nearly equal, and similar to those of CTTS (Herbig & Soderblom 1980; Hamann & Persson 1992).

From these photometric and spectroscopic observational results, we suggest that V899 Mon almost finished the outburst starting from 2012 and now returning to the CTTS stage where the mass accretion rate is lower than in the burst stage.

##### 4.2. Classification of V899 Mon

V899 Mon shows spectral features of both FUors and EXors, similar to V1647 Ori (Briceño et al. 2004; Reipurth & Aspin 2004; Vacca et al. 2004; Ojha et al. 2006; Fedele et al. 2007; Ninan et al. 2013). Repetitive outbursts of relatively short duration are similar to those of V1647 Ori. In addition, the overall optical and NIR spectra of V899 Mon resembles V1647 Ori: H $\alpha$  and H $\beta$  P Cygni profiles, numerous metallic emission lines, forbidden emission lines, strong CO overtone bandhead emission, and Br $\gamma$  emission.

V1647 Ori was classified as a “peculiar” object according to the NIR spectroscopic classification criteria (Connelley & Reipurth 2018). Peculiar objects have some spectroscopic or photometric characteristics similar to bonafide FUors. Based on their parameters to classify FUors, V899 Mon would be closer to a peculiar object than a bonafide FUor because of CO bandhead emission features, no water absorption features around the H band, and many metallic emission lines. In order to compare V899 Mon with the classification of Connelley

**Table 4.** EW of Spectral Lines

Transition	Wavelength ( $\mu\text{m}$ )	V899 Mon (Å)	EX Lup <sup>a</sup> (Å)
[Fe II]	1.6440	$-3.22 \pm 0.09$	$-3.14 \pm 0.45$
Na I	2.2062	$-1.01 \pm 0.06$	$-1.02 \pm 0.25$
Na I	2.2090	$-0.89 \pm 0.05$	$-1.18 \pm 0.22$
H <sub>2</sub> 1-0 S(1)	2.1218	$-0.23 \pm 0.05$	$-0.22 \pm 0.23$
Br $\gamma$	2.1661	$-9.29 \pm 0.12$	$-12.75 \pm 0.49$
CO 2-0	2.2935	$-24.94 \pm 0.16$	$-6.78 \pm 0.73$

<sup>a</sup>Spectrum from Kóspál et al. (2011a)

& Reipurth (2018), we measured the equivalent width (EW) of CO bandhead, Na I 2.202  $\mu\text{m}$ , Br $\gamma$  2.166  $\mu\text{m}$ , H<sub>2</sub> 2.122  $\mu\text{m}$ , and [Fe II] 1.644  $\mu\text{m}$ . The measured EWs are listed in Table 4. The EW of CO was obtained between 2.292 to 2.320  $\mu\text{m}$  because this feature is located at the edge of the order. Na I doublet lines are resolved, so we measured the EW of each line and used the total EW of the two lines. However, Ca I lines are indiscernible in our observation. V899 Mon shows rich emission spectrum similar to that of EX Lup during the outburst stage (Kóspál et al. 2011a), so the EWs of EX Lup were also measured. The measured EWs of Na I + Ca I vs. CO are located closer to peculiar objects (including V1647 Ori) and EX Lup rather than FUors and FUor-like objects (see Figure 9 in Connelley & Reipurth 2018). In addition, in the EW plot of Br $\gamma$  vs. CO (Figure 22), V899 Mon shows similarity to EX Lup rather than FUors and FUor-like objects. Overall, our photometric and spectroscopic data in the current stage of V899 Mon shows more similarities to EXors.

#### 5. CONCLUSION

We conducted photometric monitoring and spectroscopic observations of V899 Mon. Using our observations and archival data, we were able to monitor the changes in the physical properties of V899 Mon as the outburst progressed. The primary results obtained in this study are as follows:

1. The peak of the first outburst occurred in 2010 and then the star went through a relatively quick quiescent phase in 2011. After that, in 2012, the second brightening started. The second peak of the outburst was reached in 2018. Since then, the brightness of V899 Mon is gradually decreasing with an approximate rate of  $0.30 \pm 0.02 \text{ mag yr}^{-1}$ .

2. We find that the amplitude of the in-seasonal brightness variations (superimposed on the major light plateau caused by viscous heating of the disk due to enhanced accretion) between 2012 and 2016 is about

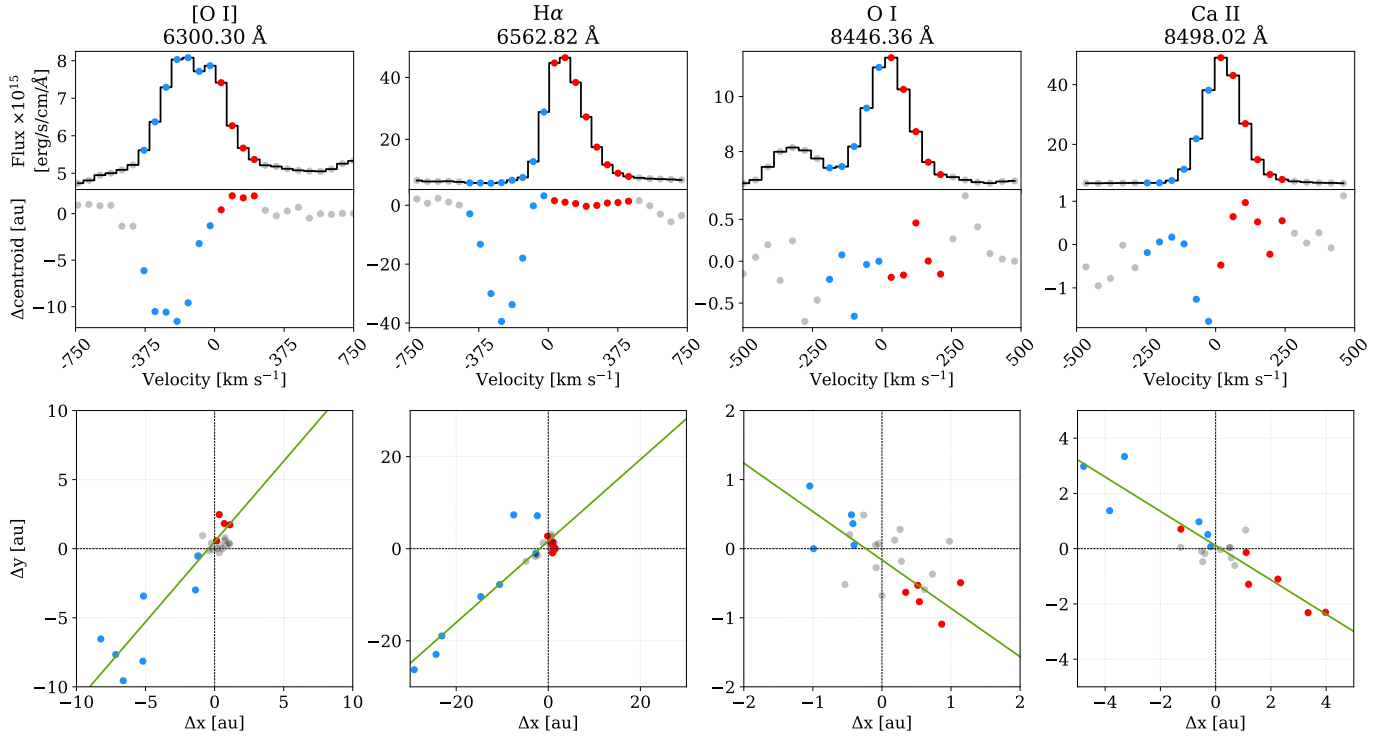


**Figure 21.** Representative spectro-astrometry data of [O I] 6300 Å, H $\alpha$  6563 Å, O I 8446 Å, and Ca II 8498 Å. Top panels show line profiles. Middle panels show the offset of the line+continuum signal regarding the continuum emission centroid. Bottom panels show 2D plot of spectro-astrometric offsets at each position and the position angle (green line). The upper and lower directions are North and South, and the left and right directions are East and West.

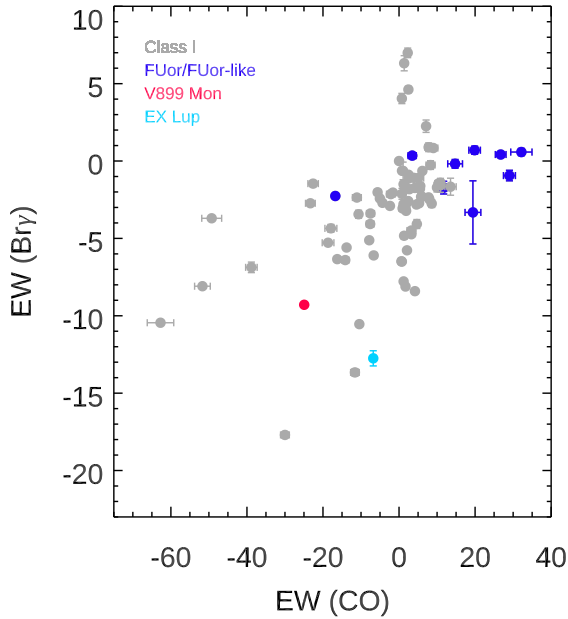


**Figure 22.** The EW of Br $\gamma$  vs. CO. Gray and blue symbols indicate Class I and FUor/FUor-like objects from Connelley & Greene (2010). Red and sky blue symbols represent V899 Mon and EX Lup, respectively. V899 Mon falls close to EX Lup, compared to FUors/FUor-like objects.

0.1 mag. Then, the amplitude became higher, about 0.2 mag, and the variations started to be dominated by accretion bursts and dips (a few of them per year were detected). The most dramatic,  $\Delta V \approx 1$  mag strong burst occurred in the 2017/2018 season, and it lasted for about 200 days. Then, again a shorter (about 30 days long) and weaker ( $\Delta V \approx 0.3$  mag) accretion burst was observed in 2020/2021. The accretion flow originating from a disk warp formed at different distances from the star can be responsible for these short accretion bursts and associated central dips. In the case of other bursts, either too sparse data, or optically thin properties of the funnel flow, or different geometry of visibility prevented us from seeing the central brightness dips. The increasing number of accretion bursts (typical for ordinary CTTS and low massive Herbig Ae stars) in parallel with the disk brightness decrease suggests that V899 Mon is gradually switching from the still not well understood accretion mechanism during the enhanced accretion (possibly a boundary layer mechanism) to the magnetospheric accretion mechanism.

3. When comparing the line profiles observed while in outburst to those compared with our observations, we found the blue-shifted absorption component of P Cygni profiles became weaker in H $\alpha$  and Ca II IRT lines, in-

dicating that the strength of outflowing wind became weaker.

4. Numerous forbidden emission lines are detected, and the estimated outflow temperature and density are about 9000 K and  $> 10^4 \text{ cm}^{-3}$ , respectively. In contrast to the weakening of the outflowing wind in P Cygni profiles, the outflow temperature and density have not changed much.

5. The estimated mass accretion rate and the mass loss rate during the fading stage are about  $10^{-7} M_{\odot} \text{ yr}^{-1}$  and  $10^{-8} M_{\odot} \text{ yr}^{-1}$ , respectively. These values are about one order of magnitude lower than those of the outbursting stage (Ninan et al. 2015), implying the weakening outburst, similar to those of CTTS. Moreover, our measured mass accretion rate is similar to that of the EX Lup during the outburst (Aspin et al. 2010).

6. Many metallic emission lines and individual CO rovibrational lines show double-peaked profiles characteristics of Keplerian rotation. In order to derive the geometrical and physical parameters of the disk, we calculated a simple disk model and estimated the disk parameters. The derived stellar mass ( $M_* \sim 2 M_{\odot}$ ) is similar to that of Ninan et al. (2015), but the obtained inclination ( $i \sim 52^\circ$ ) is higher than face-on (Ninan et al. 2016), consistent with the ALMA observation (Kóspál et al. 2021).

7. Our spectro-astrometry data shows both outflow and disk signatures. The outflowing velocity is similar to that found from the blue-shifted absorption component of H $\alpha$  P Cygni profile and extended towards the southeast. Disk signatures that are almost perpendicular to the outflow direction were also observed and distributed in the Northeast-Southwest. The disk size is consistent with that of disk modeling for the permitted metallic lines.

8. The small amplitude of photometric variations, rich emission lines, measured mass accretion rate, and mass loss rate show similar properties to those of CTTS. In addition to these properties, the gradual decreasing of the brightness indicates that V899 Mon is almost finishing its second outburst, and now it is on the way back to the quiescent phase.

9. Our recent photometric and spectroscopic observations of V899 Mon in the current evolutionary stage show more features typical for EXors.

## ACKNOWLEDGMENTS

This work used the Immersion Grating Infrared Spectrometer (IGRINS) that was developed under a collaboration between the University of Texas at Austin and the Korea Astronomy and Space Science Institute (KASI) with the financial support of the Mt. Cuba Astronomical Foundation, of the US National Science Foundation under grants AST-1229522 and AST-1702267, of the McDonald Observatory of the University of Texas at Austin, of the Korean GMT Project of KASI, and Gemini Observatory. This work was supported by K-GMT Science Program (PID: GS-2020B-Q-218) of Korea Astronomy and Space Science Institute (KASI). We gratefully acknowledge the work of the observers, Róbert Szakáts, Eda Sonbaş, and Hüseyin Er. This project has received funding from the European Research Council (ERC) under the European Union’s Horizon 2020 research and innovation programme under grant agreement No 716155 (SACCRED), and from the “Transient Astrophysical Objects” GINOP 2.3.2-15-2016-00033 project of the National Research, Development and Innovation Office (NKFIH), Hungary, funded by the European Union. ZsMSz is supported by the ÚNKP-20-2 New National Excellence Program of the Ministry for Innovation and Technology from the source of the National Research, Development and Innovation Fund. L. Kriskovics is supported by the Bolyai János Research Scholarship of the Hungarian Academy of Sciences. L. Kriskovics acknowledges the financial support of the Hungarian National Research, Development and Innovation Office grant NKFIH PD-134784. This paper uses observations made at the South African Astronomical Observatory (SAAO) and at the Mount Suhora Astronomical Observatory.

*Facilities:* Gemini:South,VLT:Yepun

*Software:* IRAF (Tody 1986, 1993)

Table 5. Photometry of V899 Mon

HJD	$U$	$B$	$g'$	$V$	$r'$	$R_C$	$i'$	$I_C$	$z'$	Obs/Tel
2458082.531	...	14.788±0.022	...	13.392±0.009	...	12.433±0.009	...	11.445±0.012	...	Konkoly/Schmidt
2458085.493	...	14.010±0.011	...	12.737±0.015	...	11.880±0.006	...	10.949±0.005	...	Konkoly/Schmidt
2459114.624	...	16.446±0.009	...	14.998±0.002	14.336±0.005	...	13.627±0.003	...	...	Konkoly/RC80
2459115.590	...	16.435±0.044	...	14.935±0.014	14.280±0.012	...	13.571±0.005	...	...	Konkoly/RC80
2459116.599	...	16.365±0.018	...	...	...	...	...	...	...	Konkoly/RC80
2459117.579	...	16.383±0.050	...	14.886±0.050	14.250±0.050	...	13.653±0.050	...	...	Konkoly/RC80
2459182.537	...	...	15.705±0.017	...	14.373±0.008	...	13.664±0.012	...	...	Adiyaman/ADYU60
2459183.452	...	...	15.849±0.029	...	14.415±0.013	...	13.716±0.014	...	...	Adiyaman/ADYU60
2459185.403	...	16.527±0.033	...	15.108±0.008	14.420±0.010	...	13.732±0.009	...	...	Konkoly/RC80
2459193.499	...	...	15.721±0.004	...	...	...	...	...	...	Mount Suhora
2459195.462	...	...	15.704±0.009	...	14.432±0.009	...	13.716±0.011	...	...	Mount Suhora
2459200.502	18.121±0.066	16.461±0.006	...	14.981±0.005	...	...	...	13.060±0.004	...	SAAO/Lesedi
2459201.357	17.841±0.038	16.459±0.005	...	14.992±0.006	...	14.079±0.007	...	13.081±0.006	...	SAAO/Lesedi
2459202.342	17.871±0.047	16.428±0.005	...	14.943±0.003	...	14.024±0.008	...	13.028±0.006	...	SAAO/Lesedi
2459203.337	17.739±0.045	16.364±0.004	...	14.908±0.006	...	14.000±0.006	...	12.995±0.005	...	SAAO/Lesedi
2459204.488	...	...	15.463±0.005	...	14.165±0.004	...	13.461±0.008	...	...	Mount Suhora
2459206.324	17.646±0.050	16.299±0.006	...	14.848±0.005	...	13.949±0.007	...	12.957±0.004	...	SAAO/Lesedi
2459207.342	17.723±0.059	16.284±0.013	...	14.838±0.008	...	13.927±0.008	...	12.938±0.005	...	SAAO/Lesedi
2459208.432	17.863±0.072	16.326±0.007	...	14.859±0.006	...	13.949±0.008	...	12.970±0.005	...	SAAO/Lesedi
2459208.806	17.434±0.020	...	15.511±0.007	...	14.198±0.007	...	13.496±0.016	...	13.017±0.014	VST/OMEGACAM
2459209.333	17.627±0.068	16.286±0.011	...	14.831±0.005	...	13.925±0.007	...	12.943±0.006	...	SAAO/Lesedi
2459210.335	17.638±0.096	16.381±0.156	...	14.922±0.009	...	14.021±0.006	...	13.033±0.004	...	SAAO/Lesedi
2459210.452	...	...	15.573±0.006	...	14.268±0.005	...	13.549±0.008	...	...	Mount Suhora
2459211.313	17.803±0.068	16.521±0.020	...	15.031±0.006	...	14.112±0.008	...	13.106±0.011	...	SAAO/Lesedi
2459212.304	...	16.508±0.012	...	15.030±0.006	...	14.119±0.007	...	13.133±0.006	...	SAAO/Lesedi
2459212.658	18.138±0.086	...	15.771±0.021	...	14.442±0.021	...	13.715±0.027	...	13.218±0.020	VST/OMEGACAM
2459213.312	18.039±0.137	16.628±0.051	...	15.121±0.012	...	14.194±0.016	...	13.202±0.013	...	SAAO/Lesedi
2459213.803	18.696±0.747	...	15.825±0.023	...	14.455±0.016	...	13.739±0.025	...	13.259±0.016	VST/OMEGACAM
2459214.296	...	16.438±0.012	...	14.933±0.018	...	14.031±0.010	...	13.032±0.006	...	SAAO/Lesedi
2459216.476	...	...	15.513±0.007	...	14.214±0.004	...	13.495±0.007	...	...	Mount Suhora
2459217.767	17.343±0.078	...	15.564±0.026	...	14.256±0.021	...	13.549±0.029	...	13.041±0.015	VST/OMEGACAM
2459218.432	...	...	15.507±0.005	...	14.219±0.004	...	13.508±0.007	...	...	Mount Suhora
2459225.387	...	...	15.692±0.005	...	14.408±0.005	...	13.690±0.012	...	...	Adiyaman/ADYU60
2459235.410	17.947±0.027	16.472±0.009	...	14.986±0.007	...	14.073±0.008	...	13.080±0.007	...	SAAO/Lesedi
2459237.463	17.880±0.101	16.458±0.008	...	15.021±0.008	...	14.128±0.012	...	13.116±0.007	...	SAAO/Lesedi
2459239.412	17.895±0.103	16.466±0.033	...	15.030±0.052	...	14.120±0.027	...	13.096±0.044	...	SAAO/Lesedi
2459241.388	17.920±0.107	16.530±0.034	...	15.020±0.011	...	14.108±0.014	...	13.096±0.005	...	SAAO/Lesedi
2459251.217	...	...	15.701±0.009	...	14.383±0.006	...	13.686±0.013	...	...	Adiyaman/ADYU60
2459252.214	...	...	15.715±0.008	...	14.397±0.007	...	13.695±0.009	...	...	Adiyaman/ADYU60
2459258.196	...	...	15.758±0.009	...	14.399±0.009	...	13.679±0.029	...	...	Adiyaman/ADYU60
2459269.223	...	...	15.629±0.043	...	14.363±0.013	...	13.637±0.010	...	...	Mount Suhora
2459272.338	...	16.413±0.076	...	15.045±0.005	14.403±0.011	...	13.687±0.006	...	...	RC80
2459273.447	...	...	...	14.907±0.010	14.338±0.010	...	13.549±0.010	...	...	RC80
2459274.305	...	16.360±0.021	...	14.952±0.008	14.322±0.003	...	13.614±0.002	...	...	RC80
2459275.373	...	16.285±0.006	...	14.894±0.014	14.273±0.004	...	13.585±0.002	...	...	RC80
2459276.328	...	16.298±0.031	...	14.921±0.016	14.317±0.004	...	13.603±0.004	...	...	RC80
2459276.343	...	...	15.600±0.006	...	14.293±0.003	...	13.566±0.007	...	...	Mount Suhora
2459278.211	...	...	15.659±0.005	...	14.355±0.004	...	13.654±0.010	...	...	Adiyaman/ADYU60
2459279.207	...	...	15.680±0.006	...	14.387±0.004	...	13.691±0.010	...	...	Adiyaman/ADYU60
2459280.335	...	16.402±0.016	...	15.005±0.014	14.378±0.007	...	13.683±0.004	...	...	RC80
2459281.288	...	...	15.625±0.014	...	14.346±0.008	...	13.643±0.013	...	...	Adiyaman/ADYU60
2459281.373	...	16.356±0.005	...	14.986±0.014	14.348±0.009	...	13.678±0.010	...	...	RC80
2459282.223	...	...	15.666±0.008	...	14.389±0.005	...	13.685±0.009	...	...	Adiyaman/ADYU60
2459284.337	...	16.507±0.022	...	15.081±0.039	14.448±0.019	...	13.704±0.002	...	...	RC80
2459298.284	...	16.374±0.033	...	14.974±0.030	14.320±0.003	...	13.585±0.005	...	...	RC80
2459299.279	...	16.239±0.021	...	14.863±0.013	14.274±0.012	...	13.555±0.005	...	...	RC80

NOTE—More information about the telescopes and instruments can be found in Section 2.1.

## APPENDIX

### A. PHOTOMETRY OF V899 MON

Table 5 shows the ground-based optical photometry we obtained for V899 Mon.

### B. SYSTEMIC VELOCITY OF V899 MON FROM ALMA OBSERVATIONS

V899 Mon was observed as part of ALMA project 2016.1.00209.S (PI: Takami). The observations include

the J=2–1 transitions of  $^{12}\text{CO}$ ,  $^{13}\text{CO}$  and  $\text{C}^{18}\text{O}$  using two ALMA configurations plus the ACA, resulting in



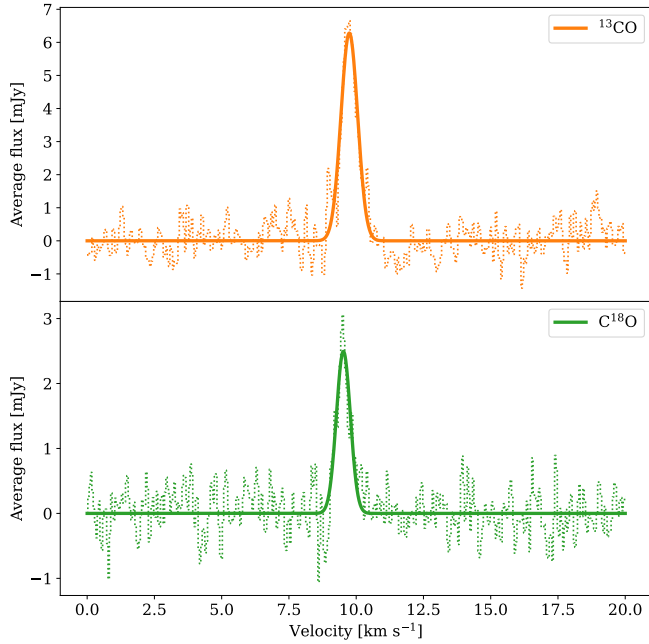


**Figure 23.** Line profiles of  $^{13}\text{CO}$  (top panel) and  $\text{C}^{18}\text{O}$  (bottom panel) observations with ALMA. The light dotted lines represent the flux averaged from a  $2''$  aperture centered on the position of the star. The thick continuum lines are the best fitted Gaussians used to determine the systemic velocity.

an angular resolution of  $\sim 0.15''$  and a maximum recoverable scale of  $29''$ . We manually calibrated the data, applied self-calibration using the two continuum spectral windows and generated data cube for the three isotopologues using the CASA package version 6.1 (McMullin et al. 2007). Exploring the three data cubes we found  $^{12}\text{CO}$  is optically thick while the other two isotopologues are optically thin and trace the gas surrounding our target. We used a  $2''$  aperture centered on the position of V899 Mon to extract the line profile, we fitted a Gaussian function to it, and determined the systemic velocity is the velocity of the peak of the best-fit. The resulting velocities are  $9.74 \text{ km s}^{-1}$  and  $9.52 \text{ km s}^{-1}$  for  $^{13}\text{CO}$  and  $\text{C}^{18}\text{O}$ , respectively. Thus we estimate the systemic velocity of V899 Mon is  $9.63 \pm 0.11 \text{ km s}^{-1}$ .

### C. SPECTRAL LINES OF V899 MON

In Figures 24–26, we provide the spectral lines of atomic hydrogen and  $\text{H}_2$  lines.

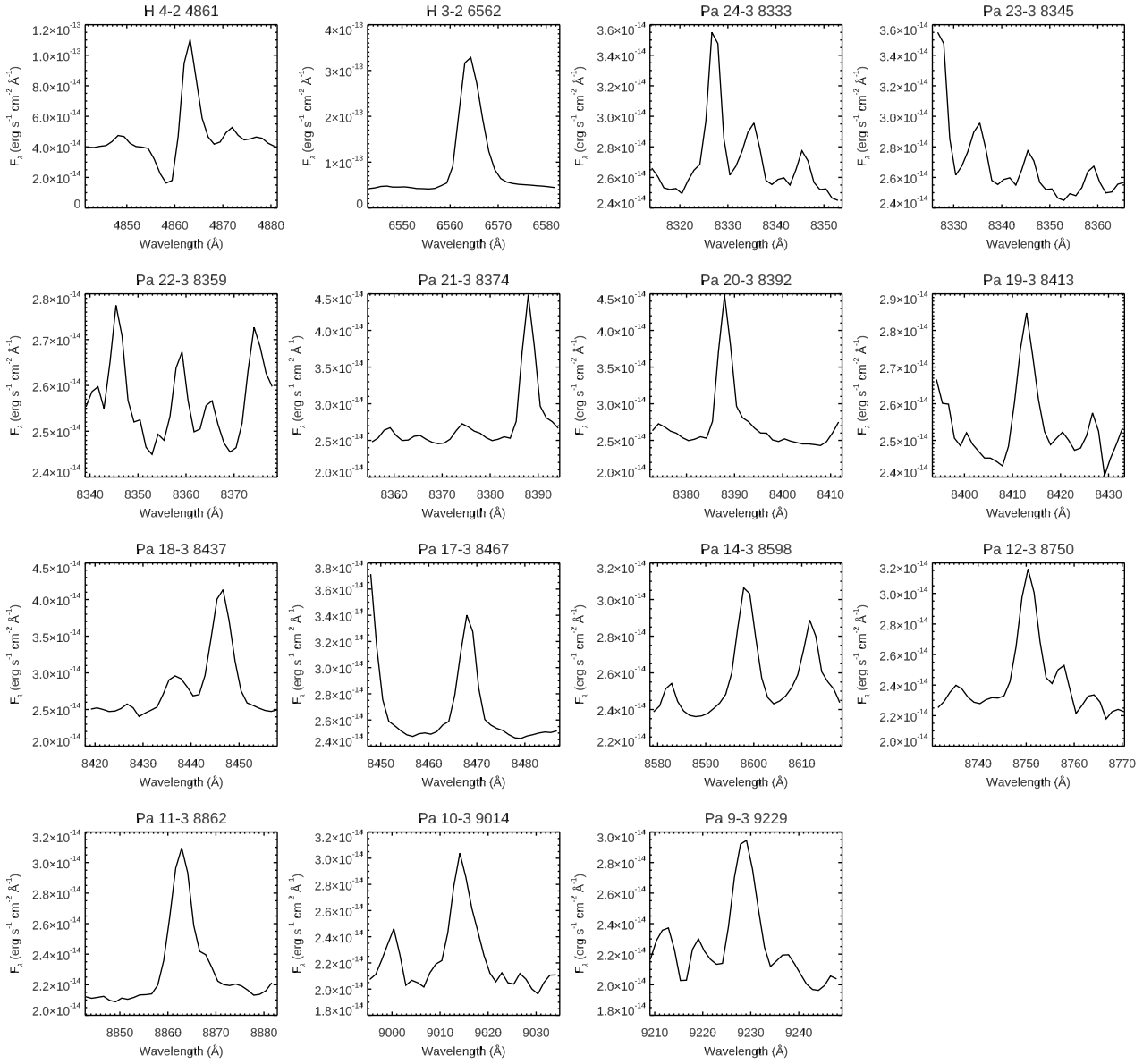


**Figure 24.** Hydrogen lines observed in the optical band.

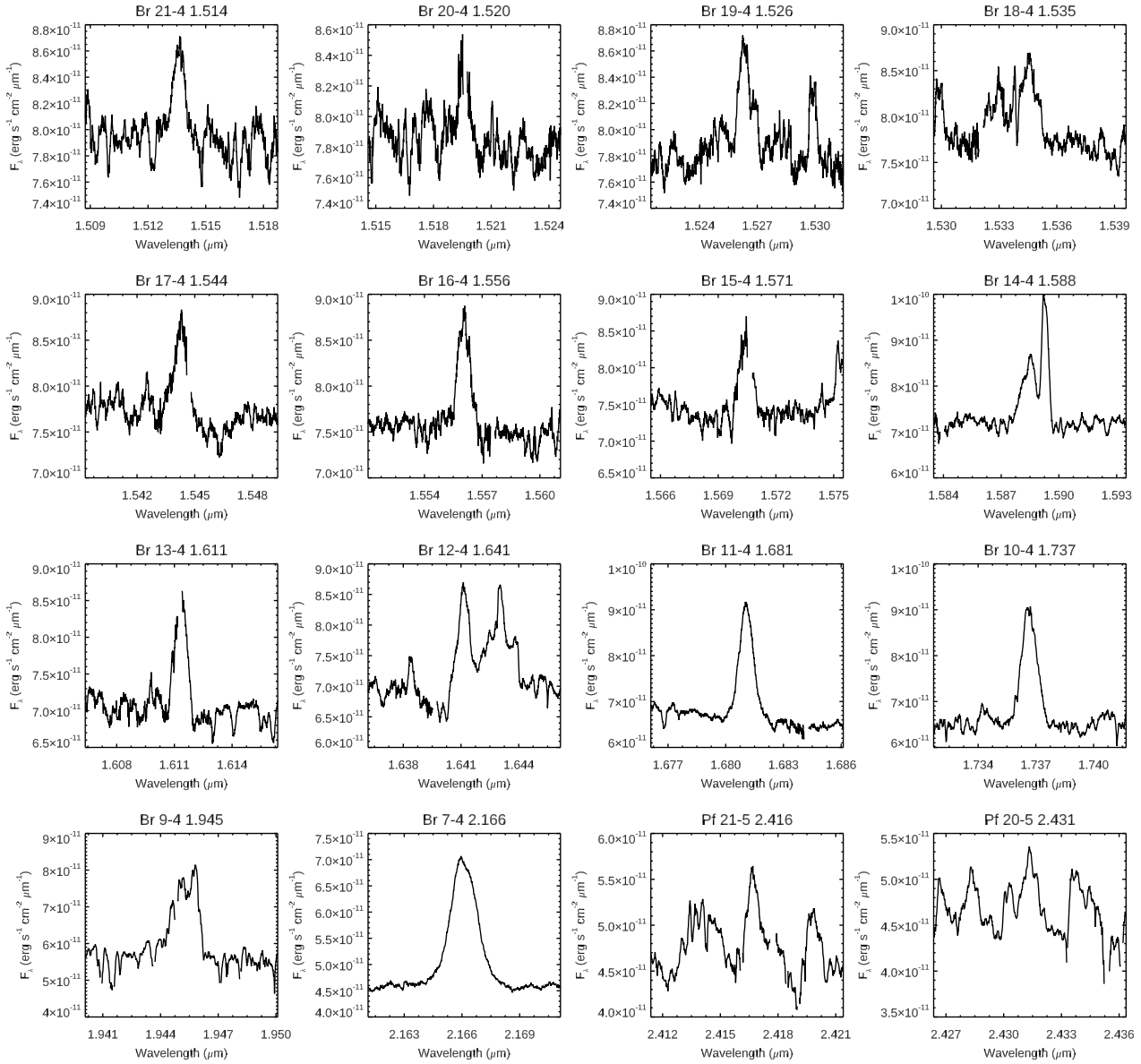


Figure 25. Hydrogen lines observed in the NIR.

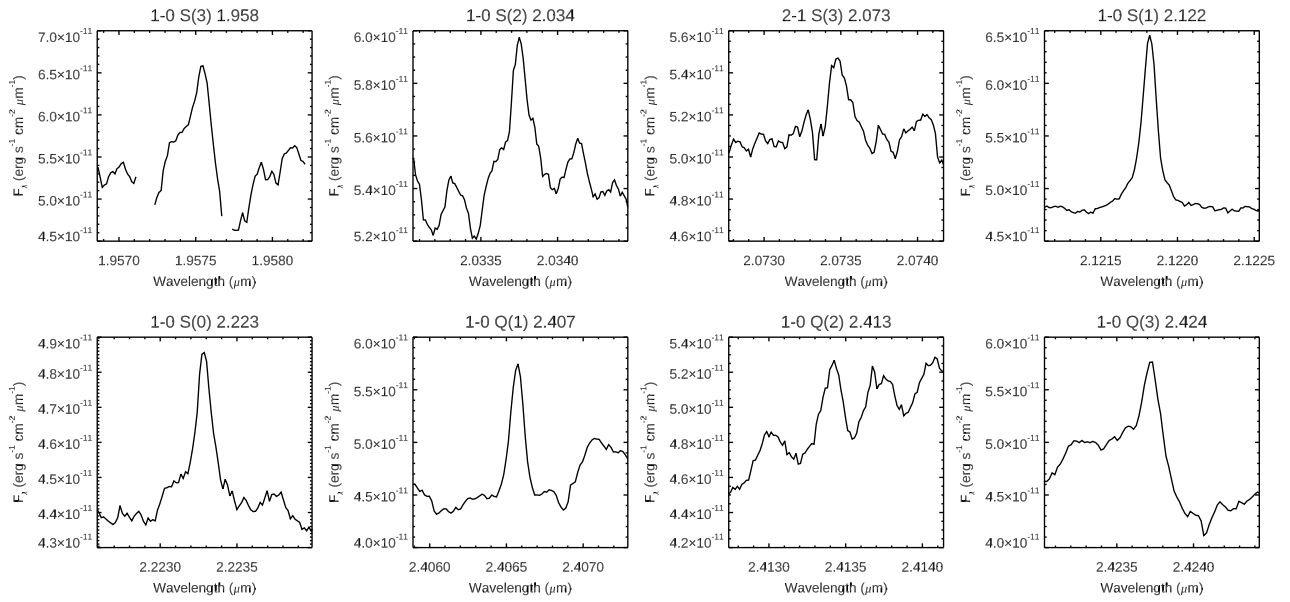


Figure 26. Molecular hydrogen lines.

## REFERENCES

- Alcalá, J. M., Manara, C. F., Natta, A., et al. 2017, *A&A*, 600, A20, doi: [10.1051/0004-6361/201629929](https://doi.org/10.1051/0004-6361/201629929)
- Arsenault, R., Madec, P. Y., Hubin, N., et al. 2008, in Society of Photo-Optical Instrumentation Engineers (SPIE) Conference Series, Vol. 7015, Adaptive Optics Systems, ed. N. Hubin, C. E. Max, & P. L. Wizinowich, 701524, doi: [10.1117/12.790359](https://doi.org/10.1117/12.790359)
- Aspin, C. 2011, *AJ*, 142, 135, doi: [10.1088/0004-6256/142/4/135](https://doi.org/10.1088/0004-6256/142/4/135)
- Aspin, C., Reipurth, B., Herczeg, G. J., & Capak, P. 2010, *ApJL*, 719, L50, doi: [10.1088/2041-8205/719/1/L50](https://doi.org/10.1088/2041-8205/719/1/L50)
- Audard, M., Ábrahám, P., Dunham, M. M., et al. 2014, in Protostars and Planets VI, ed. H. Beuther, R. S. Klessen, C. P. Dullemond, & T. Henning, 387, doi: [10.2458/azu\\_uapress\\_9780816531240-ch017](https://doi.org/10.2458/azu_uapress_9780816531240-ch017)
- Azevedo, R., Calvet, N., Hartmann, L., et al. 2006, *A&A*, 456, 225, doi: [10.1051/0004-6361:20054315](https://doi.org/10.1051/0004-6361:20054315)
- Bacon, R., Accardo, M., Adjali, L., et al. 2010, in Society of Photo-Optical Instrumentation Engineers (SPIE) Conference Series, Vol. 7735, Ground-based and Airborne Instrumentation for Astronomy III, ed. I. S. McLean, S. K. Ramsay, & H. Takami, 773508, doi: [10.1117/12.856027](https://doi.org/10.1117/12.856027)
- Bally, J. 2016, *ARA&A*, 54, 491, doi: [10.1146/annurev-astro-081915-023341](https://doi.org/10.1146/annurev-astro-081915-023341)
- Bally, J., Reipurth, B., & Davis, C. J. 2007, in Protostars and Planets V, ed. B. Reipurth, D. Jewitt, & K. Keil, 215
- Banzatti, A., Pascucci, I., Edwards, S., et al. 2019, *ApJ*, 870, 76, doi: [10.3847/1538-4357/aaf1aa](https://doi.org/10.3847/1538-4357/aaf1aa)
- Beck, T. L., McGregor, P. J., Takami, M., & Pyo, T.-S. 2008, *ApJ*, 676, 472, doi: [10.1086/527528](https://doi.org/10.1086/527528)
- Blinova, A. A., Romanova, M. M., & Lovelace, R. V. E. 2016, *MNRAS*, 459, 2354, doi: [10.1093/mnras/stw786](https://doi.org/10.1093/mnras/stw786)
- Briceño, C., Vivas, A. K., Hernández, J., et al. 2004, *ApJL*, 606, L123, doi: [10.1086/421395](https://doi.org/10.1086/421395)
- Cardelli, J. A., Clayton, G. C., & Mathis, J. S. 1989, *ApJ*, 345, 245, doi: [10.1086/167900](https://doi.org/10.1086/167900)
- Connelley, M. S., & Greene, T. P. 2010, *AJ*, 140, 1214, doi: [10.1088/0004-6256/140/5/1214](https://doi.org/10.1088/0004-6256/140/5/1214)
- Connelley, M. S., & Reipurth, B. 2018, *The Astrophysical Journal*, 861, 145, doi: [10.3847/1538-4357/aaba7b](https://doi.org/10.3847/1538-4357/aaba7b)
- Cutri, R. M., Skrutskie, M. F., van Dyk, S., et al. 2003, *VizieR Online Data Catalog*, II/246
- Cutri, R. M., Mainzer, A., Conrow, T., et al. 2015, Explanatory Supplement to the NEOWISE Data Release Products, Explanatory Supplement to the NEOWISE Data Release Products
- Davis, C. J., Gell, R., Khanzadyan, T., Smith, M. D., & Jenness, T. 2010, *A&A*, 511, A24, doi: [10.1051/0004-6361/200913561](https://doi.org/10.1051/0004-6361/200913561)
- Davis, C. J., Smith, M. D., Stern, L., Kerr, T. H., & Chiar, J. E. 2003, *MNRAS*, 344, 262, doi: [10.1046/j.1365-8711.2003.06820.x](https://doi.org/10.1046/j.1365-8711.2003.06820.x)
- Davis, C. J., Cervantes, B., Nisini, B., et al. 2011, *A&A*, 528, A3, doi: [10.1051/0004-6361/201015897](https://doi.org/10.1051/0004-6361/201015897)
- Dunham, M. M., Evans, Neal J., I., Terebey, S., Dullemond, C. P., & Young, C. H. 2010, *ApJ*, 710, 470, doi: [10.1088/0004-637X/710/1/470](https://doi.org/10.1088/0004-637X/710/1/470)
- Ellerbroek, L. E., Podio, L., Kaper, L., et al. 2013, *A&A*, 551, A5, doi: [10.1051/0004-6361/201220635](https://doi.org/10.1051/0004-6361/201220635)
- Fedele, D., van den Ancker, M. E., Petr-Gotzens, M. G., & Rafanelli, P. 2007, *A&A*, 472, 207, doi: [10.1051/0004-6361:20077725](https://doi.org/10.1051/0004-6361:20077725)
- Fernandes, A. J. L. 2000, *MNRAS*, 315, 657, doi: [10.1046/j.1365-8711.2000.03437.x](https://doi.org/10.1046/j.1365-8711.2000.03437.x)
- Foster, G. 1996, *AJ*, 112, 1709, doi: [10.1086/118137](https://doi.org/10.1086/118137)
- Gaia Collaboration, Brown, A. G. A., Vallenari, A., et al. 2021, *A&A*, 649, A1, doi: [10.1051/0004-6361/202039657](https://doi.org/10.1051/0004-6361/202039657)
- Greene, T. P., Barsony, M., & Weintraub, D. A. 2010, *ApJ*, 725, 1100, doi: [10.1088/0004-637X/725/1/1100](https://doi.org/10.1088/0004-637X/725/1/1100)
- Greene, T. P., Wilking, B. A., Andre, P., Young, E. T., & Lada, C. J. 1994, *ApJ*, 434, 614, doi: [10.1086/174763](https://doi.org/10.1086/174763)
- Gullbring, E., Barwig, H., Chen, P. S., Gahm, G. F., & Bao, M. X. 1996, *A&A*, 307, 791
- Gullbring, E., Hartmann, L., Briceño, C., & Calvet, N. 1998, *ApJ*, 492, 323, doi: [10.1086/305032](https://doi.org/10.1086/305032)
- Hamann, F. 1994, *ApJS*, 93, 485, doi: [10.1086/192064](https://doi.org/10.1086/192064)
- Hamann, F., & Persson, S. E. 1992, *ApJS*, 82, 247, doi: [10.1086/191715](https://doi.org/10.1086/191715)
- Hartigan, P., Edwards, S., & Ghandour, L. 1995, *ApJ*, 452, 736, doi: [10.1086/176344](https://doi.org/10.1086/176344)
- Hartman, J. D., & Bakos, G. A. 2016, *Astronomy and Computing*, 17, 1, doi: [10.1016/j.ascom.2016.05.006](https://doi.org/10.1016/j.ascom.2016.05.006)
- Hartmann, L. 2009, *Accretion Processes in Star Formation: Second Edition*
- Hartmann, L., & Kenyon, S. J. 1996, *ARA&A*, 34, 207, doi: [10.1146/annurev.astro.34.1.207](https://doi.org/10.1146/annurev.astro.34.1.207)
- Henden, A. A., Levine, S., Terrell, D., & Welch, D. L. 2015, in American Astronomical Society Meeting Abstracts, Vol. 225, American Astronomical Society Meeting Abstracts #225, 336.16
- Herbig, G. H. 2007, *AJ*, 133, 2679, doi: [10.1086/517494](https://doi.org/10.1086/517494)
- . 2008, *AJ*, 135, 637, doi: [10.1088/0004-6256/135/2/637](https://doi.org/10.1088/0004-6256/135/2/637)
- Herbig, G. H., Petrov, P. P., & Duemmler, R. 2003, *ApJ*, 595, 384, doi: [10.1086/377194](https://doi.org/10.1086/377194)

- Herbig, G. H., & Soderblom, D. R. 1980, *ApJ*, 242, 628, doi: [10.1086/158499](https://doi.org/10.1086/158499)
- Herczeg, G. J., Dong, S., Shappee, B. J., et al. 2016, *The Astrophysical Journal*, 831, 133, doi: [10.3847/0004-637x/831/2/133](https://doi.org/10.3847/0004-637x/831/2/133)
- Hillenbrand, L. A., Reipurth, B., Connelley, M., Cutri, R. M., & Isaacson, H. 2019, *AJ*, 158, 240, doi: [10.3847/1538-3881/ab4e16](https://doi.org/10.3847/1538-3881/ab4e16)
- Hirth, G. A., Mundt, R., & Solf, J. 1997, *A&AS*, 126, 437, doi: [10.1051/aas:1997275](https://doi.org/10.1051/aas:1997275)
- Hodapp, K. W., Reipurth, B., Pettersson, B., et al. 2019, *AJ*, 158, 241, doi: [10.3847/1538-3881/ab471a](https://doi.org/10.3847/1538-3881/ab471a)
- Hodapp, K. W., Denneau, L., Tucker, M., et al. 2020, *AJ*, 160, 164, doi: [10.3847/1538-3881/abad96](https://doi.org/10.3847/1538-3881/abad96)
- Hummer, D. G., & Storey, P. J. 1987, *MNRAS*, 224, 801, doi: [10.1093/mnras/224.3.801](https://doi.org/10.1093/mnras/224.3.801)
- Kenyon, S. J., Hartmann, L. W., Strom, K. M., & Strom, S. E. 1990, *AJ*, 99, 869, doi: [10.1086/115380](https://doi.org/10.1086/115380)
- Kochanek, C. S., Shappee, B. J., Stanek, K. Z., et al. 2017, *PASP*, 129, 104502, doi: [10.1088/1538-3873/aa80d9](https://doi.org/10.1088/1538-3873/aa80d9)
- Kóspál, Á., Ábrahám, P., Carmona, A., et al. 2020, *ApJL*, 895, L48, doi: [10.3847/2041-8213/ab93d4](https://doi.org/10.3847/2041-8213/ab93d4)
- Kóspál, Á., Szabó, Z. M., Ábrahám, P., et al. 2020, *The Astrophysical Journal*, 889, 148, doi: [10.3847/1538-4357/ab6174](https://doi.org/10.3847/1538-4357/ab6174)
- Kóspál, Á., Ábrahám, P., Goto, M., et al. 2011a, *ApJ*, 736, 72, doi: [10.1088/0004-637X/736/1/72](https://doi.org/10.1088/0004-637X/736/1/72)
- Kóspál, Á., Ábrahám, P., Acosta-Pulido, J. A., et al. 2011b, *A&A*, 527, A133, doi: [10.1051/0004-6361/201016160](https://doi.org/10.1051/0004-6361/201016160)
- Kóspál, Á., Cruz-Sáenz de Miera, F., White, J. A., et al. 2021, arXiv e-prints, arXiv:2106.14409. <https://arxiv.org/abs/2106.14409>
- Kraus, M., Krügel, E., Thum, C., & Geballe, T. R. 2000, *A&A*, 362, 158. <https://arxiv.org/abs/astro-ph/0008213>
- Lee, J.-E., Park, S., Green, J. D., et al. 2015, *ApJ*, 807, 84, doi: [10.1088/0004-637X/807/1/84](https://doi.org/10.1088/0004-637X/807/1/84)
- Lee, J.-J., & Gullikson, K. 2017, *igrins/plp v2.2.0-alpha.4*, doi: [10.5281/zenodo.438353](https://doi.org/10.5281/zenodo.438353)
- Lorenzetti, D., Larionov, V. M., Giannini, T., et al. 2009, *ApJ*, 693, 1056, doi: [10.1088/0004-637X/693/2/1056](https://doi.org/10.1088/0004-637X/693/2/1056)
- Mace, G., Kim, H., Jaffe, D. T., et al. 2016, in *Society of Photo-Optical Instrumentation Engineers (SPIE) Conference Series*, Vol. 9908, *Ground-based and Airborne Instrumentation for Astronomy VI*, ed. C. J. Evans, L. Simard, & H. Takami, 99080C, doi: [10.1117/12.2232780](https://doi.org/10.1117/12.2232780)
- Mainzer, A., Bauer, J., Grav, T., et al. 2011, *ApJ*, 731, 53, doi: [10.1088/0004-637X/731/1/53](https://doi.org/10.1088/0004-637X/731/1/53)
- Mainzer, A., Bauer, J., Cutri, R. M., et al. 2014, *ApJ*, 792, 30, doi: [10.1088/0004-637X/792/1/30](https://doi.org/10.1088/0004-637X/792/1/30)
- Masci, F. J., Laher, R. R., Rusholme, B., et al. 2018, *Publications of the Astronomical Society of the Pacific*, 131, 018003, doi: [10.1088/1538-3873/aae8ac](https://doi.org/10.1088/1538-3873/aae8ac)
- McMullin, J. P., Waters, B., Schiebel, D., Young, W., & Golap, K. 2007, in *Astronomical Society of the Pacific Conference Series*, Vol. 376, *Astronomical Data Analysis Software and Systems XVI*, ed. R. A. Shaw, F. Hill, & D. J. Bell, 127
- Muzerolle, J., Hartmann, L., & Calvet, N. 1998, *AJ*, 116, 455, doi: [10.1086/300428](https://doi.org/10.1086/300428)
- Ninan, J. P., Ojha, D. K., Bhatt, B. C., et al. 2013, *The Astrophysical Journal*, 778, 116, doi: [10.1088/0004-637x/778/2/116](https://doi.org/10.1088/0004-637x/778/2/116)
- Ninan, J. P., Ojha, D. K., & Philip, N. S. 2016, *The Astrophysical Journal*, 825, 65, doi: [10.3847/0004-637x/825/1/65](https://doi.org/10.3847/0004-637x/825/1/65)
- Ninan, J. P., Ojha, D. K., Baug, T., et al. 2015, *The Astrophysical Journal*, 815, 4, doi: [10.1088/0004-637x/815/1/4](https://doi.org/10.1088/0004-637x/815/1/4)
- Nisini, B., Caratti o Garatti, A., Giannini, T., & Lorenzetti, D. 2002, *A&A*, 393, 1035, doi: [10.1051/0004-6361:20021062](https://doi.org/10.1051/0004-6361:20021062)
- Nisini, B., Milillo, A., Saraceno, P., & Vitali, F. 1995, *A&A*, 302, 169
- Ojha, D. K., Ghosh, S. K., Tej, A., et al. 2006, *MNRAS*, 368, 825, doi: [10.1111/j.1365-2966.2006.10159.x](https://doi.org/10.1111/j.1365-2966.2006.10159.x)
- Park, C., Jaffe, D. T., Yuk, I.-S., et al. 2014, in *Proc. SPIE*, Vol. 9147, *Ground-based and Airborne Instrumentation for Astronomy V*, 91471D, doi: [10.1117/12.2056431](https://doi.org/10.1117/12.2056431)
- Park, S., Lee, J.-E., Kang, W., et al. 2018, *ApJS*, 238, 29, doi: [10.3847/1538-4365/aadd14](https://doi.org/10.3847/1538-4365/aadd14)
- Park, S., Lee, J.-E., Pyo, T.-S., et al. 2020, *ApJ*, 900, 36, doi: [10.3847/1538-4357/aba532](https://doi.org/10.3847/1538-4357/aba532)
- Petrov, P. P., & Herbig, G. H. 2008, *AJ*, 136, 676, doi: [10.1088/0004-6256/136/2/676](https://doi.org/10.1088/0004-6256/136/2/676)
- Press, W. H. 1978, *Comments on Astrophysics*, 7, 103
- Pyo, T.-S., Kobayashi, N., Hayashi, M., et al. 2003, *ApJ*, 590, 340, doi: [10.1086/374966](https://doi.org/10.1086/374966)
- Reipurth, B., & Aspin, C. 2004, *ApJL*, 606, L119, doi: [10.1086/421393](https://doi.org/10.1086/421393)
- Ricker, G. R., Winn, J. N., Vanderspek, R., et al. 2015, *Journal of Astronomical Telescopes, Instruments, and Systems*, 1, 014003, doi: [10.1117/1.JATIS.1.1.014003](https://doi.org/10.1117/1.JATIS.1.1.014003)
- Rigliaco, E., Gratton, R., Kóspál, Á., et al. 2020, *A&A*, 641, A33, doi: [10.1051/0004-6361/202038337](https://doi.org/10.1051/0004-6361/202038337)
- Rucinski, S. M., Zwintz, K., Hareter, M., et al. 2010, *A&A*, 522, 8, doi: [10.1051/0004-6361/201014856](https://doi.org/10.1051/0004-6361/201014856)
- Shappee, B. J., Prieto, J. L., Grupe, D., et al. 2014, *ApJ*, 788, 48, doi: [10.1088/0004-637X/788/1/48](https://doi.org/10.1088/0004-637X/788/1/48)
- Shu, F. H. 1977, *ApJ*, 214, 488, doi: [10.1086/155274](https://doi.org/10.1086/155274)

- Sicilia-Aguilar, A., Kóspál, Á., Setiawan, J., et al. 2012, *A&A*, 544, A93, doi: [10.1051/0004-6361/201118555](https://doi.org/10.1051/0004-6361/201118555)
- Sipos, N., Ábrahám, P., Acosta-Pulido, J., et al. 2009, *A&A*, 507, 881, doi: [10.1051/0004-6361/200911641](https://doi.org/10.1051/0004-6361/200911641)
- Siwak, M., Ogloza, W., Moffat, A. F. J., et al. 2018, *MNRAS*, 478, 758, doi: [10.1093/mnras/sty1220](https://doi.org/10.1093/mnras/sty1220)
- Smith, M. D. 1995, *A&A*, 296, 789
- Stauffer, J., Cody, A. M., Baglin, A., et al. 2014, *AJ*, 147, 83, doi: [10.1088/0004-6256/147/4/83](https://doi.org/10.1088/0004-6256/147/4/83)
- Ströbele, S., La Penna, P., Arsenault, R., et al. 2012, in *Society of Photo-Optical Instrumentation Engineers (SPIE) Conference Series*, Vol. 8447, *Adaptive Optics Systems III*, ed. B. L. Ellerbroek, E. Marchetti, & J.-P. Véran, 844737, doi: [10.1117/12.926110](https://doi.org/10.1117/12.926110)
- Tody, D. 1986, in *Society of Photo-Optical Instrumentation Engineers (SPIE) Conference Series*, Vol. 627, *Instrumentation in astronomy VI*, ed. D. L. Crawford, 733, doi: [10.1117/12.968154](https://doi.org/10.1117/12.968154)
- Tody, D. 1993, in *Astronomical Society of the Pacific Conference Series*, Vol. 52, *Astronomical Data Analysis Software and Systems II*, ed. R. J. Hanisch, R. J. V. Brissenden, & J. Barnes, 173
- Turner, J., Kirby-Docken, K., & Dalgarno, A. 1977, *ApJS*, 35, 281, doi: [10.1086/190481](https://doi.org/10.1086/190481)
- Vacca, W. D., Cushing, M. C., & Simon, T. 2004, *ApJL*, 609, L29, doi: [10.1086/422638](https://doi.org/10.1086/422638)
- van den Ancker, M. E., Wesselius, P. R., Tielens, A. G. G. M., van Dishoeck, E. F., & Spinoglio, L. 1999, *A&A*, 348, 877
- Weilbacher, P. M., Palsa, R., Streicher, O., et al. 2020, *A&A*, 641, A28, doi: [10.1051/0004-6361/202037855](https://doi.org/10.1051/0004-6361/202037855)
- Wils, P., Greaves, J., Catelan, M., et al. 2009, *The Astronomer's Telegram*, 2307, 1
- Wright, E. L., Eisenhardt, P. R. M., Mainzer, A. K., et al. 2010, *AJ*, 140, 1868, doi: [10.1088/0004-6256/140/6/1868](https://doi.org/10.1088/0004-6256/140/6/1868)
- Wright, J. T., & Eastman, J. D. 2014, *PASP*, 126, 838, doi: [10.1086/678541](https://doi.org/10.1086/678541)
- Yershov, V. N. 2014, *Ap&SS*, 354, 97, doi: [10.1007/s10509-014-1944-5](https://doi.org/10.1007/s10509-014-1944-5)
- Yuk, I.-S., Jaffe, D. T., Barnes, S., et al. 2010, in *Proc. SPIE*, Vol. 7735, *Ground-based and Airborne Instrumentation for Astronomy III*, 77351M, doi: [10.1117/12.856864](https://doi.org/10.1117/12.856864)
- Zechmeister, M., & Kürster, M. 2009, *A&A*, 496, 577, doi: [10.1051/0004-6361:200811296](https://doi.org/10.1051/0004-6361:200811296)
- Zhu, Z., Espaillat, C., Hinkle, K., et al. 2009, *ApJL*, 694, L64, doi: [10.1088/0004-637X/694/1/L64](https://doi.org/10.1088/0004-637X/694/1/L64)